Journal of Materials Chemistry B

Dual Amyloid Cross-Seeding Reveals Steric Zipper-Facilitated Fibrillization and Pathological Links between Protein Misfolding Diseases

Journal:	*Journal of Materials Chemistry B*
Manuscript ID	TB-ART-12-2020-002958.R1
Article Type:	Paper
Date Submitted by the Author:	08-Feb-2021
Complete List of Authors:	Zhang, Yanxian; University of Akron, Chemical and Biomolecular Engineering Zhang, Mingzhen; University of Akron, Chemical and Biochemical Engineering Liu, Yonglan; University of Akron, Chemical and Biomolecular Engineering Zhang, Dong; University of Akron, Chemical, Biomolecular, and Corrosion Engineering; University of Akron, Tang, Yijing; University of Akron, Chemical and Biomolecular Engineering Ren, Baiping; Dalian University of Technology, School of Life Science and Biotechnology Zheng, Jie; University of Akron, Chemical and Biomolecular Engineering

Dual Amyloid Cross-Seeding Reveals Steric Zipper-Facilitated Fibrillization and Pathological Links between Protein Misfolding Diseases

Yanxian Zhang[1ζ], Mingzhen Zhang[1ζ], Yonglan Liu[1ζ], Dong Zhang[1], Yijing Tang[1], Baiping Ren[1], and Jie Zheng[1*]

[1]Department of Chemical, Biomolecular, and Corrosion Engineering
The University of Akron, Ohio, USA

[ζ] These authors contribute equally to this work.

* Corresponding author: zhengj@uakron.edu

Abstract

Amyloid cross-seeding, as a result of direct interaction and co-aggregation between different disease-causative peptides, is considered as a main mechanism for the spread of the overlapping pathology across different cells and tissues between different protein-misfolding diseases (PMDs). Despite biomedical significance of amyloid cross-seeding in amyloidogenesis, it remains a great challenge to discover amyloid cross-seeding systems and reveal their cross-seeding structures and mechanisms. Herein, we are the first to report that GNNQQNY – a short fragment from yeast prion protein Sup35 – can cross-seed with both amyloid-β (Aβ, associated with Alzheimer's disease) and human islet amyloid polypeptide (hIAPP, associated with type II diabetes) to form β-structure-rich assemblies and to accelerate amyloid fibrillization. Dry, steric β-zippers, formed by the two β-sheets of different amyloid peptides, provide generally interactive and structural motifs to facilitate amyloid cross-seeding. The presence of different steric β-zippers in a variety of GNNQQNY-Aβ and GNNQQNY-hIAPP assemblies also explains amyloid polymorphism. In addition, alteration of steric zipper formation by single-point mutations of GNNQQNY and interactions of GNNQQNY with different Aβ and hIAPP seeds leads to different amyloid cross-seeding efficiencies, further confirming the existence of cross-seeding barriers. This work offers a better structural-based understanding of amyloid cross-seeding mechanisms linked to different PMDs.

Keywords: GNNQQNY, Amyloid cross-seeding, Amyloid aggregation, Amyloid-β, hIAPP, Alzheimer's disease, Type II diabetes, Prion disease

1. Introduction

The aggregation of the same misfolded amyloid proteins into β-structure-rich fibrils (i.e., amyloid homologous-seeding) is well recognized as the common pathological hallmarks of many protein misfolding diseases (PMDs) including Alzheimer's disease (AD), type II diabetes (T2D), and prion disease[1-6]. Different from amyloid homologous-seeding that is solely associated with a specific PMD, co-aggregation of different amyloid proteins (i.e., amyloid cross-seeding), such as Aβ and α-synuclein[7], Aβ and tau[8], Aβ and transthyretin[9], hIAPP and insulin[10], have been found in patients with several PMDs. Another major difference from amyloid homologous-seeding is that not any two different amyloid proteins enable cross-seeding behaviors.[11-13] This indicates the existence of certain amyloid cross-seeding barriers along the co-aggregation pathways of different amyloid proteins[14, 15]. Moreover, amyloid cross-seeding is more fundamentally and biologically important for not only the pathological process of each PMD, but also the potential molecular cross-talk between different PMDs, which could be a main mechanism for the spread of the overlapping pathology across different cells and tissues between PMDs.[16-23] However, amyloid cross-seeding is still a subject poorly explored and little is known about its sequence/structure-dependent aggregation mechanisms[24-27].

Among different PMDs, prion amyloidosis is considered as the most transmissible disease, which not only occurs in many mammalian species including human, cow, sheep, and goat[28], but also co-occurs with other PMDs including AD, Parkinson's disease, and T2D in the same individual[29-32]. Clinical and epidemiological studies have revealed that prion aggregation increases the risk of progression and transmission of AD by 15%[20, 21], T2D [33, 34], and exacerbates diabetic strokes[35]. Similar pathological link has also been observed between AD and T2D[36]. Each of these three diseases is identified as a risk factor to elevate the incidence of the other two diseases and induce some common pathological symptoms and cell degeneration[37-40], including excess oxidative stress[41], chronic inflammation[42], and endocrine homeostasis[43]. While the exact transmission mechanism of prion disease towards AD and T2D is still unclear, mutual cross-seeds between these disease-linked amyloid proteins or amyloid-prone fragments are considerable as transmissible species through plasma and cerebrospinal fluids to reach the target cells and tissues, leading to prion-linked strains, Aβ-linked plaques, and hIAPP-linked strains[39].

Generally speaking, each PMD is associated with the aggregation of a specific amyloid protein, e.g., Aβ, hIAPP, or prion aggregation is associated with AD, T2D, or prion disease, respectively. While Aβ, hIAPP, and prion have different sequences and native functions, they all adopt common cross-β structures upon aggregation. Particularly, some amyloid-prone fragments from Aβ, hIAPP, and prion, including GNNQQNY from the yeast prion Sup35[44, 45], KLVFFAE, NKGAII, GGVVIA from Aβ[46-48], and NFGAIL, SSTNVG, NFLVHSS, NVGSNTY from hIAPP[49, 50] can self-aggregate into amyloid-like fibrils, which are conformationally similar to their parent proteins[51]. Among them, $GNNQQNY_{sup35}$[52-54], $KLVFFA_{A\beta}$[55], $NKGAII_{A\beta}$[48], $GGVVIA_{A\beta}$[47], $NFGAIL_{hIAPP}$[56], $SSTNVG_{hIAPP}$, and $NVGSNTY_{hIAPP}$[57] can also form steric zippers between β-sheets, whose sidechains from the β-sheets are interdigitated against each other to stabilize the

self-assembled structures. Sequence analysis also reveals high occurrence of Asn/Gln/aromatic residues in these three amyloid proteins (**Fig. S1**), providing a higher possibility for them to form stacked amino acid ladders[58]. Hypothetically, such common β-sheet steric zippers, as observed from different amyloid proteins, may offer a structural basis for amyloid cross-seeding between GNNQQNY-Aβ and GNNQQNY-hIAPP via non-covalent steric zipper interactions.

To test the steric-zipper driven cross-seeding hypothesis, herein we are the first to study the amyloid cross-seeding of GNNQQNY with both full-length $A\beta_{42}$ and $hIAPP_{37}$ on the basis of potential pathological transmission between prion disease, AD, and T2D. First, collective aggregation and structural results showed that GNNQQNY can indeed cross-seed both Aβ and hIAPP to accelerate amyloid fibrillization and to form β-structure-rich assemblies, as compared to Aβ or hIAPP aggregation alone. Second, we developed a simulation platform to determine a structural ensemble of GNNQQNY-Aβ and GNNQQNY-hIAPP assemblies with polymorphic double- and triple-layer organizations. While GNNQQNY-Aβ/hIAPP assemblies displayed different structural organizations in terms of β-sheet–to–β-sheet orientations and packings, they all formed steric-zipper interfaces between different but complement β-sheets from GNNQQNY and Aβ or hIAPP. Elimination of these steric-zipper interactions by single-point mutations of GNNQQNY reduced its cross-seeding ability to Aβ or hIAPP, highlighting the importance of steric β-zippers in amyloid cross-seeding. Third, *in vitro* cell assays showed that the cross-seeds of GNNQQNY-Aβ and GNNQQNY-hIAPP reduced the respective Aβ-induced and hIAPP-induced toxicity against mammalian cells. Taken together, these findings, for the first time, discovered GNNQQNY as a dual cross-seeding peptide to promote amyloid fibrillization of both Aβ and hIAPP via steric zipper interactions, which may explain molecular cross-talk between these PMDs as attributed by the spread of prion propagation in the pathologies of patients with AD and T2D.

2. Results

Before cross-seeding tests, we first conducted a control study to investigate the self-aggregation of GNNQQNY, a seven-residue fragment from a yeast prion protein of Sup35, into β-structure-rich fibrils. Thioflavin-T (ThT) fluorescence experiments in **Fig. S2a** showed the concentration-dependent aggregation behavior of GNNQQNY under quiescent conditions. Specifically, GNNQQNY did not aggregate into amyloid fibrils at the low concentrations of 10-15 μM, as evidenced by flat ThT curves without obvious changes around 15 a.u. during 24 h incubation. However, at concentrations of 20-25 μM GNNQQNY showed a slow increase of aggregation, while at concentrations of above 50 μM, GNNQQNY showed typical sigmoidal fibrillization curves starting from a very short lag phase, a gradual increased growth phase, to a final equilibrium phase. This fibrilization trend became more pronounced and faster at higher GNNQQNY concentrations. Meanwhile, both AFM and CD data confirmed the formation of GNNQQNY amyloid-like fibrils with β-sheet structure at the higher concentrations of 125 μM, but neither fibrils nor β-sheet structures in GNNQQNY aggregates was observed at 15 μM (**Fig. S2 b-e**).

2.1. GNNQQNY cross-seeds with Aβ to promote amyloid fibrillization

The control study of pure GNNQQNY aggregation determined a non-amyloidogenic concentration range of <15 μM, which is selected and used to study its cross-seeding behavior with Aβ and hIAPP without interference by GNNQQNY self-aggregation. It should be noted that unavoidable deviations on amyloid aggregation in different experiments (e.g., ThT, CD, SEM) might occur when using different samples. Also, the activity of peptides is somehow sensitive to environmental factors (e.g., temperature, humidity, and vibration). To avoid these potential effects, we conducted at least 3 independent replicant tests for each experiment to obtain statistically fair and valid comparisons. For the cross-seeding of GNNQQNY (15 μM) with Aβ (15 and 30 μM), ThT kinetic curves in **Fig. 1a** showed that pure Aβ at both 15 and 30 μM concentrations enabled to form amyloid fibrils, but 30 μM Aβ aggregated faster than 15 μM Aβ, as evidenced by the shorter lag phase (0.5 h vs. 1.5 h), the higher maximal ThT intensity (I_{max}=344 vs. I_{max}=207), and the less time to reach half of I_{max} (T_{50}= 3.5 h vs. T_{50}= 12.5 h). When incubating non-amylogenic GNNQQNY (15 μM) with Aβ at 1:1 and 1:2 molar ratios, GNNQQNY clearly promoted Aβ fibrillization as judged by the increase of I_{max} from 207 to 295 at 1:1 ratio and from 344 to 522 at 1:2 ratio (Aβ is 2-fold excess). Since GNNQQNY at 15 μM is not amyloidogenic, such increase of I_{max} is solely attributed to the cross-seeding of GNNQQNY with Aβ to form hybrid GNNQQNY-Aβ fibrils in a dose-dependent manner. Specifically, at GNNQQNY:Aβ molar ratio of 1:1, cross-seeding of GNNQQNY with Aβ significantly and immediately promoted the formation of hybrid oligomers and protofibrils at the growth phases and finally increased I_{max} by 42% (**Fig. 1a & 1b**). Differently, the 1:2 mixture of GNNQQNY and Aβ exhibited similar growth kinetics to pure Aβ (30 μM) during the early aggregation (0-5 h), but promoted final fibril formation by 52% at the later stage. Concentration-dependent cross-seeding effect implies different cross-seeding pathways between GNNQQNY and Aβ, i.e., the lower concentration of Aβ favor to cross-seed with GNNQQNY to form GNNQQNY-Aβ oligomers at the early stage, followed by the growth into higher-order cross-seeds and cross-fibrils. Higher concentration of Aβ, due to its fast aggregation nature, tends to form homogenous seeds with non-detectable influence by GNNQQNY, and then the dominant Aβ seeds serve as structural templates to recruit GNNQQNY monomers to form hybrid GNNQQNY-Aβ fibrils at the later aggregation stage.

In parallel, AFM images showed the morphological changes of pure Aβ (15 μM) from small spherical oligomers at 6 h, to a few short protofibrils at 12 h, and to long and dense fibrils at 24 h (**Fig. 1c**). For comparison, cross-seeding of GNNQQNY with Aβ at 1:1 molar ratio exhibited noticeable morphological changes in the size and number of oligomers, protofibrils, and mature fibrils in an increased manner. Further analysis of the cross-sectional height and width of amyloid fibrils obtained from high-resolution AFM images showed that cross-seeded GNNQQNY-Aβ fibrils had the average width/height of 13.4±0.7 nm/8.3±0.6 nm in cross-section areas, which was much higher than the 8.7±0.3 nm/5.3±0.4 nm width/height of pure fibrils (**Fig. 1d** & **1e**). The fibrillization process of Aβ with and without GNNQQNY was further monitored by the conformational structural change by CD spectroscopy. Aβ (15 μM) self-aggregation followed a typical

structural transition from random to β-sheet structure with both antiparallel and parallel organizations being equally presented after 24 h (**Fig. 1f & 1g**). When cross-seeding of GNNQQNY with Aβ at 1:1 ratio, CD spectra exhibited a different pattern in two aspects by (i) promoting the β-sheet formation by 34.5%, where the increase of β-sheet content in GNNQQNY-Aβ assemblies comes at the expense of random structure, and (ii) organizing the β-sheet packing in a preferentially antiparallel manner (100% of total β-sheet content) as shown by two negative bands at 200 nm and 220 nm and a positive band at 195 nm. Taken together, ThT, AFM, and CD results demonstrated the cross-seeding of GNNQQNY with Aβ that promoted amyloid fibrillization, and such cross-seeding-induced promotion effect mainly stems from the acceleration of conformational transition from random structure to antiparallel β-sheets.

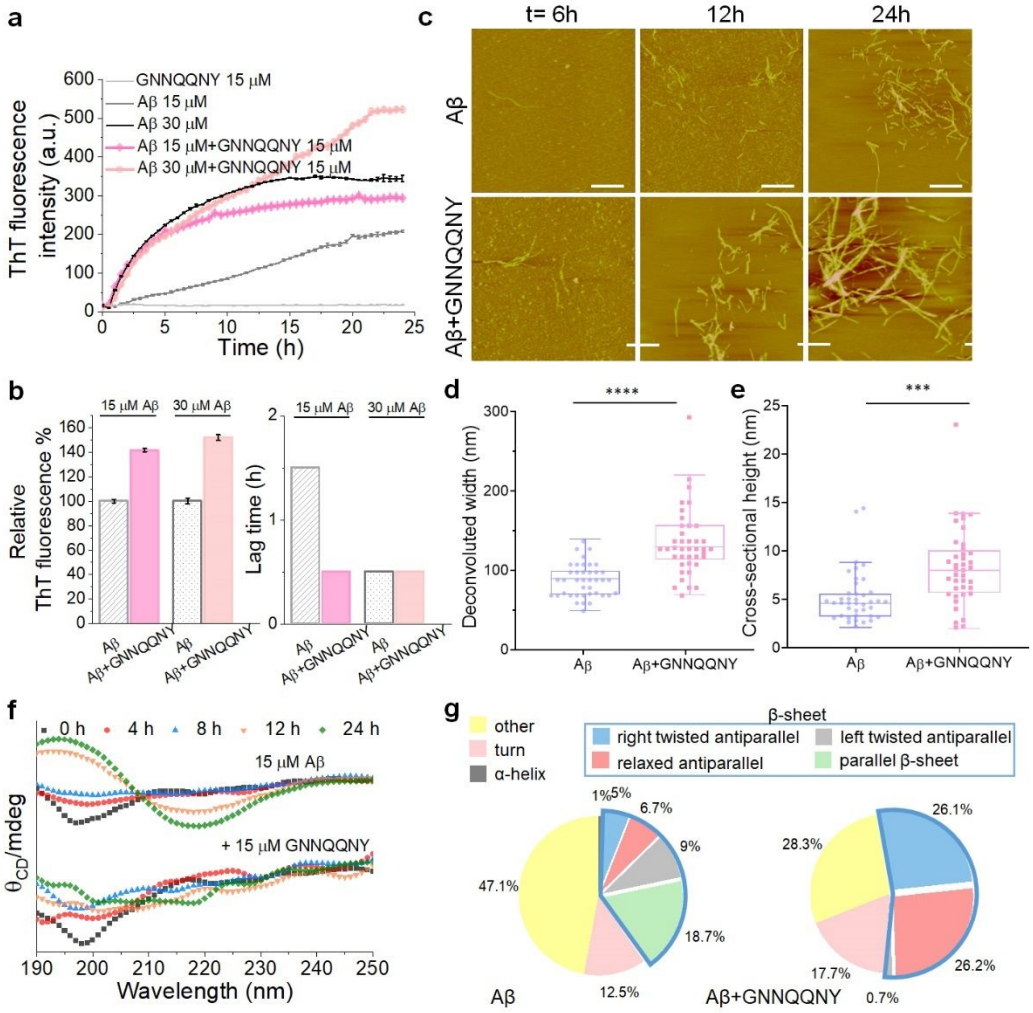

Figure 1. Cross-seeding of GNNQQNY with Aβ to promote amyloid fibrillization. a Time-dependent Thioflavin (ThT) fluorescence curves to monitor the aggregation kinetics of the cross-seeding between GNNQQNY and Aβ at 1:1 and 1:2 molar ratios, in comparison with pure Aβ aggregation. **b** Comparison of the aggregation kinetics of Aβ in the presence and absence of GNNQQNY in terms of their final fluorescence intensity and lag time. Final ThT fluorescence of pure Aβ aggregation is set to 100% and used as a basis to define the relative ThT fluorescence ratio of GNNQQNY-Aβ cross-seeding. **c** AFM images of pure Aβ (15 μM) and hybrid GNNQQNY-Aβ (15 μM:15 μM) aggregates at different aggregation times of 6, 12, and 24 h. Scale bars are 1 μm. Statistical analysis of the cross-sectional **d** width and **e** height of pure Aβ fibrils (blue) and GNNQQNY-Aβ cross-seeding fibrils (pink) at 24 h aggregation. The upper,

middle, and lower boundaries of a box define the first, the median, and third quartiles of the data, respectively, and the whiskers are plotted by the Tukey method. N=40, *P < 0.05, ***P = 0.0001, ****P < 0.0001 by t-test. **f** Circular dichroism (CD) spectra of pure Aβ (15 μM) and GNNQQNY-Aβ (15 μM:15 μM) aggregations at different times of 0, 4, 8, 12, and 24 h. **g** Secondary structure distributions of pure Aβ (15 μM) and GNNQQNY-Aβ (15 μM:15 μM) aggregates at 24 h.

2.2. GNNQQNY cross-seeds with hIAPP to promote amyloid fibrillization

The cross-seeding results of GNNQQNY and Aβ motivated us to further explore the cross-seeding possibility of GNNQQNY with hIAPP, because Aβ and hIAPP share many common characteristics, including high degrees of sequence identity (25%) and similarity (50%)[45, 46], similar U-bent structures in fibrils[59, 60], amyloid cross-seeding between them[18, 61-63], and pathological connection between AD and T2D[64, 65]. ThT kinetic curves in **Fig. 2a** showed the typical sigmoidal increase of amyloid aggregation for both pure hIAPP and GNNQQNY-hIAPP cases, consistent with the amyloid nucleation-polymerization model. The self-aggregation of hIAPP was strongly depended on its concentration, i.e., 15 μM of hIAPP exhibited the longer lag phase, the slower growth phase, and the lower ThT fluorescence intensity than 30 μM of hIAPP during the entire aggregation process. Addition of 15 μM of GNNQQNY to both hIAPP solutions of different concentrations indeed promoted their aggregation, especially at the growth and equilibrium phases. I_{max} was increased by ~100% at 1:1 ratio and ~135% at 1:2 ratio, relative to I_{max} of the corresponding hIAPP aggregation alone (**Fig. 2b**). AFM images in **Fig. 2c** also showed that the cross-seeding samples of GNNQQNY-hIAPP exhibited more and highly dense aggregates than pure hIAPP samples at each aggregation stage, consistent with ThT results. Further side-by-side size comparison of final fibrils formed by pure hIAPP and GNNQQNY-hIAPP cross-seeding revealed that self-assembled hIAPP fibrils (7.4±0.3 nm/9.2±0.8 nm) had the relative smaller width/height than cross-seeded GNNQQNY-hIAPP fibrils (13.5±0.8 nm/11.8±0.8 nm) (**Fig. 2d & 2e**).

Time-dependent CD spectra in **Fig. 2f** showed that both pure hIAPP (15 μM) and GNNQQNY-hIAPP (15 μM:15 μM) underwent similar structural transition from random coils (a representative negative minimum of ~197 nm) to a mixed α-helix and β-sheet structures (a positive peak of ~193 nm and a wide negative valley at 210-220 nm). On the other hand, peak differences in CD spectra also indicate that pure hIAPP and GNNQQNY-hIAPP fibrils present different secondary structure distributions and structural transition rates. Specifically, GNNQQNY-hIAPP fibrils contained 42.4% of antiparallel β-sheet structure and 6.9% of α-helix, as compared to 27% of mixed parallel and antiparallel β-sheet and 12.4% of α-helix in hIAPP fibrils (**Fig. 2g)**. Further CD comparison of pure and cross-seeding amyloid fibrils reveals different β-sheet packing preference, i.e., pure amyloid fibrils tend to adopt both parallel and antiparallel β-sheet packings, while cross-seeding GNNQQNY-Aβ and GNNQQNY-hIAPP fibrils favor to adopt antiparallel β-sheet packing at the expense of both α-helixes and random coils, suggesting that cross-seeding requires different interfacial interactions and structural compatibility to form such β-sheet packing between different amyloid peptides.

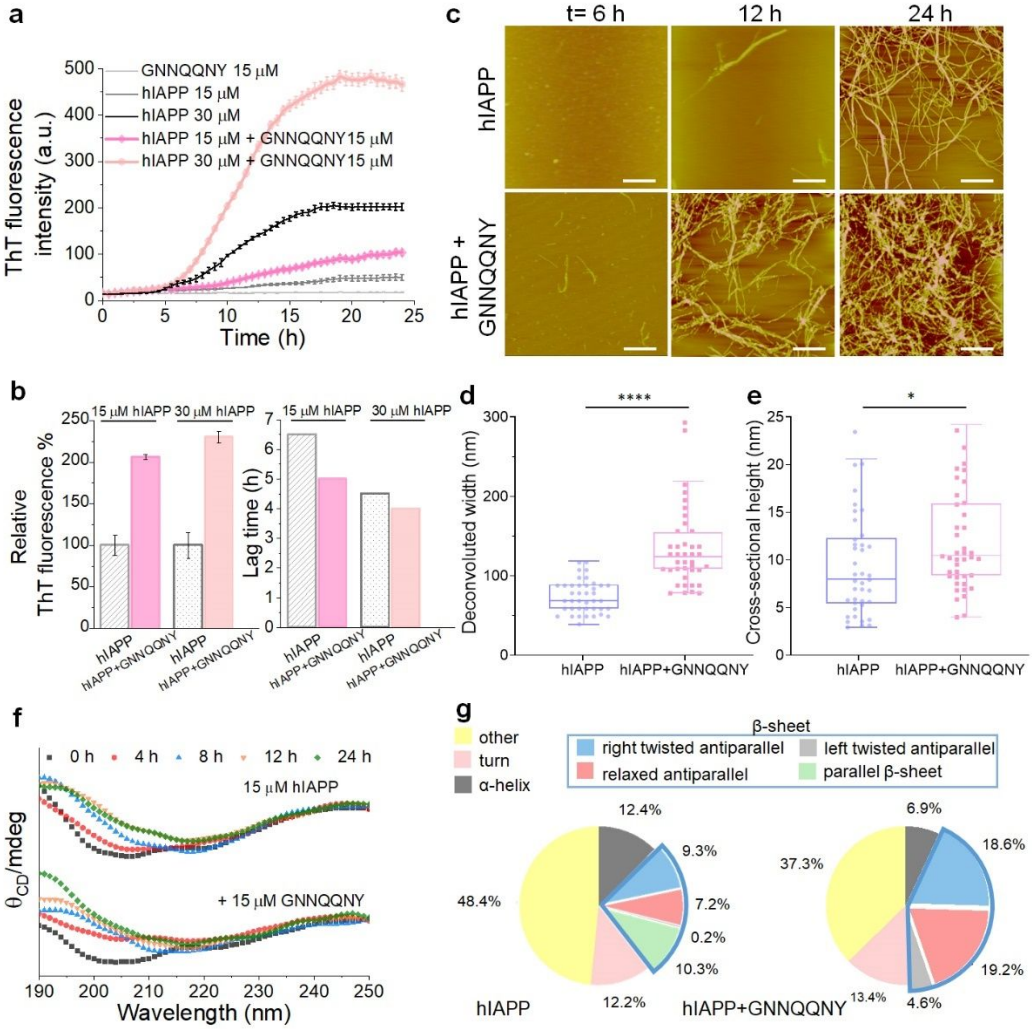

Figure 2. Cross-seeding of GNNQQNY with hIAPP to promote amyloid fibrillization. a Time-dependent Thioflavin (ThT) fluorescence curves to monitor the aggregation kinetics of the cross-seeding between GNNQQNY and hIAPP at 1:1 and 1:2 molar ratios, in comparison with pure hIAPP aggregation. **b** Comparison of the aggregation kinetics of hIAPP in the presence and absence of GNNQQNY in terms of their final fluorescence intensity and lag time. Final ThT fluorescence of pure hIAPP aggregation is set to 100% and used as a basis to define the relative ThT fluorescence ratio of GNNQQNY-hIAPP cross-seeding. **c** AFM images of pure hIAPP (15 μM) and hybrid GNNQQNY-hIAPP (15 μM:15 μM) aggregates at different aggregation times of 6, 12, and 24 h. Scale bars are 1 μm. Statistical analysis of the cross-sectional **d** width and **e** height of pure hIAPP fibrils (blue) and GNNQQNY-hIAPP cross-seeding fibrils (pink) at 24 h aggregation. The upper, middle, and lower boundaries of a box define the first, the median, and third quartiles of the data, respectively, and the whiskers are plotted in Tukey method. N=40, *P < 0.05, ***P = 0.0001, ****P < 0.0001 by *t*-test. **f** Circular dichroism (CD) spectra of pure hIAPP (15 μM) and GNNQQNY-hIAPP (15 μM:15 μM) aggregations at different times of 0, 4, 8, 12, and 24 h. **g** Secondary structure distributions of pure hIAPP (15 μM) and GNNQQNY-hIAPP (15 μM:15 μM) aggregates at 24 h.

Our findings have demonstrated, for the first time, that GNNQQNY can cross-seed with the two different amyloid proteins of Aβ and hIAPP, and effectively promote their fibrillization. On the other hand, concentration- and sequence-dependent cross-seeding behaviors also indicate the existence of energy barriers and competitive interactions

between homologous-seeding and cross-seeding, leading to different cross-seeding scenarios. In the first cross-seeding scenario, as the target amyloid protein (Aβ or hIAPP) at low concentrations undergoes the slow homologous-seeding, this allows small GNNQQNY peptides to easily adjust their conformations to accommodate with target amyloid proteins and to form cross-seeds at the early stage. Long sequence of Aβ or hIAPP makes homologous-seeding less efficiency than cross-seeding due to its much larger structural misfolding spaces. This cross-seeding scenario was observed in the cross-seeding of GNNQQNY with hIAPP or with Aβ at low concentration. Differently, when target amyloid proteins aggregate faster at high concentrations, homologous-seeding outperforms cross-seeding to form dominant homo-seeds at the early stage, which serve as structural templates to recruit GNNQQNY to further grow into high-order cross-seeds at the later aggregation stage. This second cross-seeding scenario was observed in the case of the cross-seeding of GNNQQNY with high concentration of Aβ.

2.3. GNNQQNY cross-seeds with different Aβ and hIAPP seeds to modulate the cross-seeding pathways

To further gain insights into the cross-seeding pathways between GNNQQNY and Aβ/hIAPP, we designed different cross-seeding tests by adding non-amyloidogenic GNNQQNY (15 μM) to preformed Aβ (15 μM) or hIAPP (15 μM) seeds formed at different aggregation stages, including lag phase, middle of growth phase, and early equilibrium phase. For the cross-seeding of GNNQQNY with Aβ (**Fig. 3a**), addition of GNNQQNY to 1 h Aβ seeds promoted ThT intensity significantly and immediately, indicating that Aβ seeds can efficiently cross-seed GNNQQNY and promote their aggregation, leading to an increase of final fibrils by 133% relative to pure Aβ aggregation. Further, cross-seeding of GNNQQNY with 5 h Aβ seeds at the growth phase also promoted fibril formation, but in much less efficient way, as evidenced by 13% increase of amyloid fibrils. This less cross-seeding efficiency became more pronounced when adding GNNQQNY to preformed Aβ fibrils (14 h), leading to almost no change in ThT curve. SDS-PAGE gels in **Fig. S3** reveals different aggregates formed by pure and cross-seeding amyloids. It can be seen in **Fig. S3a**, the distribution of Aβ aggregates in the absence of GNNQQNY was first presented by single band for monomers (~4.5 kDa) at 1 h, followed by two light bands for tetramers (~14 kDa) and pentamers (~18 kDa) at 4 h. The addition of GNNQQNY to Aβ solution advanced the appearance of tetrameric and pentameric bands at 1 h, which were rapidly faded away and converted into high-ordered aggregates of 150 kDa after 3 h. We also recorded the β-structure changes before and after adding GNNQQNY to Aβ seeds using CD spectra (**Fig. S4a & Fig. 3c**). Of note, since GNNQQNY mainly adopted random structures when adding it to equimolar concentration of Aβ or hIAPP, it is not surprising to observe the initial decrease of β-sheet content at the time point of GNNQQNY addition. In the case of cross-seeding of GNNQQNY with 1 h Aβ seeds, after a short period of cross-seeding, β-sheet content was rapidly increased to 50% at 12 h and remained almost unchanged after that. Differently, the cross-seeding of GNNQQNY with 5 h Aβ seeds led to a gradual and continuous increase of β-sheet content to 37% at 12 h and 47% at 24 h. More importantly, we examined the binding affinity and preference of GNNQQNY to different preformed Aβ seeds of different concentrations using SPR sensors. Briefly, GNNQQNY was covalently immobilized on

carboxymethylated dextran-modified gold SPR chips by direct amine coupling, followed by flowing different Aβ seed solutions (the detailed SPR experimental setup was described in Methods and **Fig. S5**). Comparison of SPR sensorgrams between **Fig. 3e-f** showed that the immobilized GNNQQNY adsorbed (i) more 1 h Aβ seeds than 5 h Aβ seeds at every concentration tested (1, 3.75, 7.5, and 15 μM) and (ii) more Aβ seeds of higher concentrations. Kinetic analysis further revealed that 1 h Aβ seeds exhibited a dissociation constant (K_D) of 0.9 μM, which was 7-times lower than that of 6.3 μM for 5 h Aβ seeds. This indicates that GNNQQNY binds to early Aβ seeds more strongly than to later Aβ ones.

Next, we tested whether GNNQQNY has preferentially interact with certain hIAPP seeds. It can be seen in **Fig. 3b** that after adding GNNQQNY to the 5 h seeded hIAPP solution at the lag-phase, the cross-seeding aggregation remained at lag phase for ~1 h, followed by a rapid increase of aggregation at growth phase between 6-10 h, and finally promoted fibril formation with a 96% increase in I_{max}. Differently, addition of GNNQQNY to 12 h hIAPP seeds at growth phase caused a temporary retard in the cross-seeding growth as reflected by the flat ThT intensity for additional 3 h, this indicates that large hIAPP seeds and small GNNQQNY may require longer time to mutually adjust and optimize their conformations to achieve cross-seeding. After passing this prolonged lag phase, cross-seeding gained a momentum to accelerate the aggregation, finally leading to 29% increase of amyloid fibrils. However, hIAPP mature fibrils lost its ability to cross-seed GNNQQNY, as judged by the almost same ThT kinetic curves of cross-seeding of GNNQQNY with 18 h hIAPP fibrils as that of pure hIAPP aggregation. SDS-PAGE gels in **Fig. S3b** also showed that GNNQQNY interacted with hIAPP to produce high-molecular-weight bands at 37-250 kDa, which were largely unavailable in pure hIAPP aggregates. CD spectra in **Fig. S4b** and **Fig. 3d** showed that addition of GNNQQNY to both 5 h and 12 h hIAPP seeds promoted the respective β-sheet structural conversion by 11% and 4%. Consistently, SPR results showed that GNNQQNY interacts more preferentially and strongly with 5 h hIAPP oligomeric seeds (K_D=3.2 μM, **Fig. 3g**) than 12 hIAPP protofibrillar seeds (K_D=9.0 μM, **Fig. 3h**), indicating different cross-seeding pathways.

Taken together, collective data from ThT, AFM, SDS-PAGE, CD, and SPR analyses confirm that GNNQQNY serves as a dual cross-seeding peptide to interact with both Aβ and hIAPP at monomeric, oligomeric, and protofibril states, all eventually promoting their amyloid fibrillization to different degrees. Cross-seeding of GNNQQNY with hIAPP or Aβ appears to follow the same mechanism. GNNQQNY tends to cross-seed more efficiently with small Aβ/hIAPP oligomers than large Aβ/hIAPP protofibrils, presumably due to the easier structural compatibility and the less energy barrier for small GNNQQNY to accommodate Aβ/hIAPP. Moreover, Aβ and hIAPP fibrils are less structurally active and more insoluble, making hydrophilic GNNQQNY difficult to interact with hydrophobic Aβ/hIAPP aggregates and thus reducing cross-seeding activity.

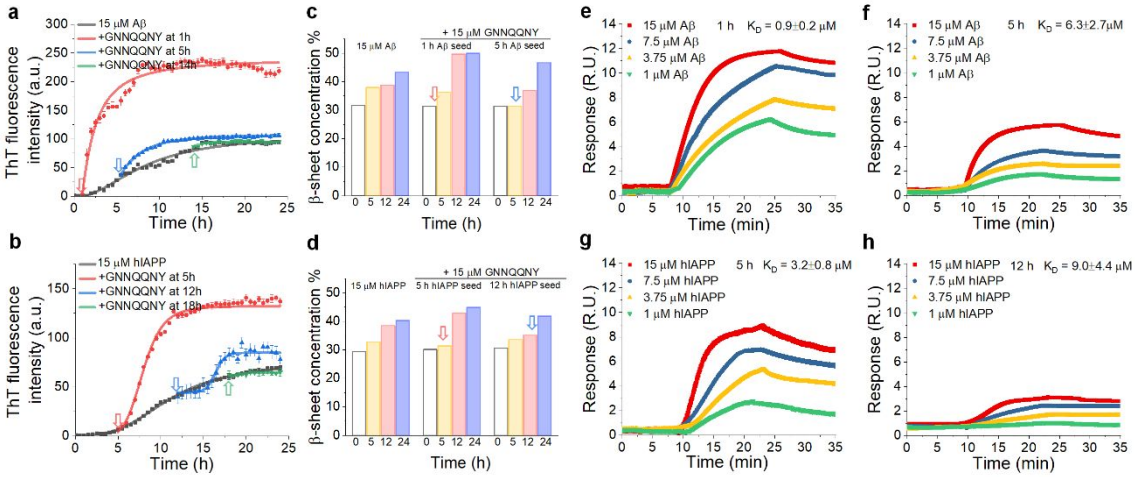

Figure 3. Cross-seeding of GNNQQNY with different Aβ and hIAPP seeds. Time-dependent ThT fluorescence curves for adding GNNQQNY (15 μM) to **a** Aβ (15 μM) and **b** hIAPP (15 μM) seeds preformed at the lag, growth, and equilibrium phases. β-sheet structure changes before and after adding GNNQQNY to **c** Aβ and **d** hIAPP seeds at different time points. SPR sensorgrams to show the binding amount and affinity of GNNQQNY to **e** 1 h Aβ seeds, **f** 5 h Aβ seeds, **g** 5 h hIAPP seeds, **h** 12 h hIAPP seeds at different concentrations. Dissociation constant (K_D) is calculated from SPR sensorgrams and shown in each panel.

2.4. Cross-seeding of GNNQQNY with Aβ and hIAPP reveals steric zippers at interfaces

To better understand molecular-level mechanism of cross-seeding of GNNQQNY with both Aβ and hIAPP, we developed a multiscale simulation platform to reveal the molecular structures, association forces, and interfacial packings of GNNQQNY-Aβ and GNNQQNY-hIAPP assemblies at atomic details. Briefly, we first applied an in-house peptide-packing program[62, 66-69] to high-throughput screen all possible cross-seeding interfaces between GNNQQNY and Aβ (or hIAPP) by considering four key parameters of interlayer translation (d_x), interlayer distance (d_y), layer-to-layer orientation (parallel vs. antiparallel), and interfacial sidechain contacts (even face *vs.* odd face of GNNQQNY) between two different amyloid assemblies (see details in Methods). As a result, a total of 2,240 GNNQQNY-Aβ and 2,400 GNNQQNY-hIAPP cross-seeding interfaces were generated and their conformational energies were evaluated to determine the most possible cross-seeding interfaces at their lowest energy states. Among them, 11 GNNQQNY-Aβ (**Fig. S6**) and 14 GNNQQNY-hIAPP (**Fig. S7**) cross-seeding interfaces were determined. At the first glance, while all of these lowest-energy cross-seeding interfaces exhibited distinct interfacial packing and orientation between two β-layers, they all adopted steric zipper structures, whose side chains are geometric complementarity to form a dry interface within the bilayer, to make the two β-sheets from different amyloid aggregates packed more closely. Since the lowest-conformation-energy structures determined by energy minimization do not necessarily imply the most stable structures in the explicit solvent due to the lack of certain explicit peptide-water interactions especially for hydrogen bonds between peptides and waters, all of 25 double-layer cross-seeding assemblies were then submitted to all-atom explicit-solvent MD simulations to truly determine their structural stability for model validation.

Throughout a total of 1,250 ns (50 ns × 25 systems=1,250 ns) MD simulations, five GNNQQNY-Aβ (A1, A3, A4, A5, and A10) and eight GNNQQNY-hIAPP (H1, H2, H3, H4, H7, H8, H9, and H13) assemblies were found to be the most structurally stable, all of which were capable for maintaining their overall β-layer association and secondary β-sheet structures, as evidenced by low RMSDs, high SASAs, no interfacial separation between the two pentamers, and no peptide disassociation within the pentamers (**Fig. S8**). Among them, **Fig. 4** presented the most populated structures of double-layer amyloid cross-seeding assemblies based on conformational energies of all constructed models. A1 (~24.9%), A3 (~20.9%), A5 (~16.3%) and A10 (~33.4%) for GNNQQNY-Aβ (**Fig. 4a**) and H3 (~19%), H4 (~16%), H7 (~12%), H9 (~11%), and H13 (~22%) for GNNQQNY-hIAPP (**Fig. 4b**) were identified as the most structurally stable and energetically favorable cross-seeding assemblies, as evidenced by their high structural stability (RMSD: ~2.6-4.4Å for GNNQQNY-Aβ, ~3.5-4.9Å for GNNQQNY-hIAPP), highly dry interface (SASA: ~150-204 $Å^2$/peptide for GNNQQNY-Aβ, ~156-214 $Å^2$/peptide for GNNQQNY-hIAPP), and high populations (~16.3-33.4% for GNNQQNY-Aβ, ~11.0%-22.0% for GNNQQNY-hIAPP). These highly structural stable and populated cross-seeding assemblies covered the longer interface with a maximum overlap of the two *β*-sheets between GNNQQNY and Aβ (or hIAPP), enabling strong interfacial interactions to stabilize well packed, dry, steric-zipper interfaces. It is interesting to note that due to highly hydrophilic and uncharged nature of GNNQQNY, the hydrophobic interactions are less important for stabilizing the cross-seeding assemblies. Instead, interfacial steric zippers formed by two tightly interdigitated β-sheets provide general driving forces to stabilize cross-seeding assemblies.

On the other hand, since all of double-layer cross-seeding assemblies presented completely different steric zippers at interfaces, they were likely stabilized by different steric zipper interactions stemmed from different interfacial residues and layer-to-layer orientations (**Table S1** and **Fig. S6-7**). Specifically, for GNNQQNY-Aβ assemblies, GNNQQNY favored to interact with the C-terminal surface of Aβ (A1, A3, A4 and A5) with the two tightly interdigitated and widely spanned β-sheets between GNNQQNY and C-terminal residues of Aβ (I31, G33, M35, G37, V39, I41, A42) (**Fig. 4a**). Meanwhile, more diverse steric zippers were observed in GNNQQNY-hIAPP assemblies with a more evenly distributed structural population ranging from ~11.0 to ~22.0%. H3, H4, H7, and H9 favored to form steric zippers with C-terminal residues of hIAPP (S29, N31, G33, N35, Y37). Additional structural differences between these steric zippers included (1) different interfacial orientations, i.e., parallel β-sheet packing in A5, A10, H7, and H9, while anti-parallel β-sheet packing in A1, A3, H3, H4 and H13; (2) different interacting faces, i.e., odd surface of GNNQQNY and C-terminal residues of Aβ or hIAPP (namely, odd-C-terminal) in A1, A5, H3, and H9, even-C-terminal in A3, H4 and H7, and even-N-terminal in A10 and H13.

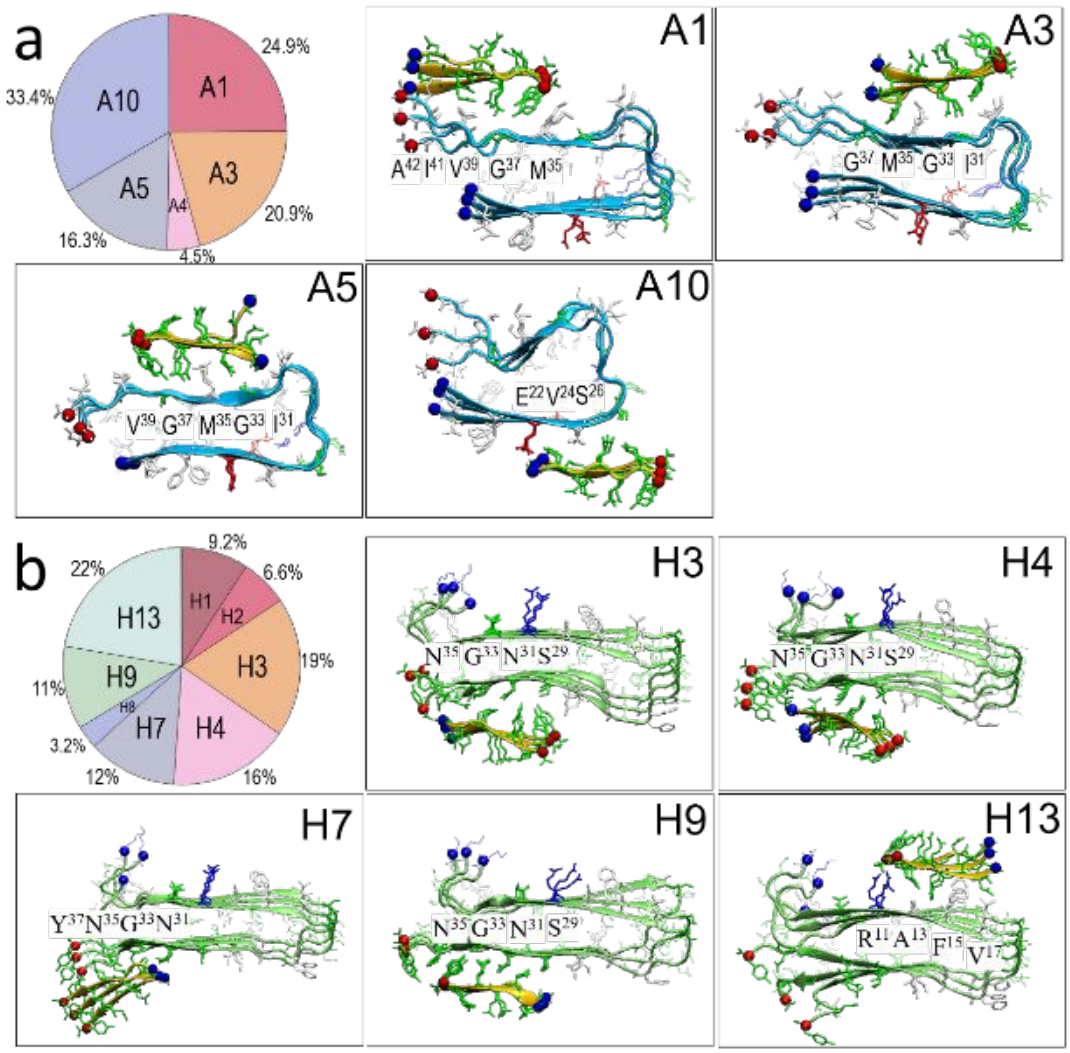

Figure 4. Highly populated and stable structures of double-layer GNNQQNY-Aβ and GNNQQNY-hIAPP assemblies. Structural populations and organizations of different steric zippers in double-layer **a** GNNQQNY-Aβ and **b** GNNQQNY-hIAPP assemblies, with different orientations and contacting residues between two β-sheets from GNNQQNY and Aβ/hIAPP.

Double-layer steric zippers in cross-seeding assemblies provide multiple possibilities to laterally assemble multiple amyloid aggregates into high-ordered, multiple-layer cross-seeding assemblies. To test this hypothesis, we constructed different sandwich-like, triple-layer cross-seeding assemblies by laterally combining two stable steric zippers (as identified in **Fig. 4**) with a GNNQQNY layer being sandwiched in between the two Aβ (or hIAPP) layers. Specifically, we constructed two triple-layer (i) Aβ-GNNQQNY-Aβ assemblies of AGA1 by combining A5 and A10 interfaces and AGA2 by combining A3 and A5 interfaces (**Fig. 5a**) and (ii) hIAPP-GNNQQNY-hIAPP assemblies of HGH1 by combining H9 and H13 interfaces and HGH2 by combining H8 and H9 interfaces (**Fig. 5b**), based on a combination criteria of structural stability, populations, contacting residues, and geometrical match. MD simulations showed that AGA1 and HGH1 outperformed its respective AGA2 and HGH2 in terms of structural stability. AGA1 and HGH1 were able to retain overall structural integrity, local secondary structure, and dry steric zipper interface, as quantified by small RMSDs of 3-5 Å, high interaction energies

of ~-600 to -800 kcal/mol, and well-preserved secondary structures (**Fig. S9**). The two steric zippers in AGA1 and HGH1 can readily accommodate three layers by rotating and translating the β-layers to adopt different favorable packings, which can greatly enrich the polymorphism of fibrils. Further structural population analysis demonstrated the co-existence of different triple-layer cross-seeding assemblies, as such 74.9% of AGA1 and 25.1% of AGA2 and 74.8% of HGH1 and 25.2% of HGH2.

A close inspection of these steric zippers in double- and triple-layer assemblies revealed an interesting steric zipper structure located at the target Aβ and hIAPP β-sheets. It can be seen in **Fig. S10** that C-terminal β-sheets of Aβ and hIAPP have completely different sequences, they both presented the similar structural motifs of X_{out}-G-X_{out} ("out" indicate that a residue of Aβ or hIAPP points outwards GNNQQNY), i.e., I31-G33-M35, M35-G37-V39 in Aβ (**Fig. 5a**) and N31-G33-N35 in hIAPP (**Fig. 5b**), which offer a large concave to accommodate the intrusion of even two long sidechains of GNNQQNY, again demonstrating that the geometrical sidechain matching in steric zippers plays an important role in determining the stability of oligomers. In a broader view, when more than three layers are stacked together, the layer-by-layer sandwich structure is likely to be less populated because the twisting of β-layer, asymmetrical stacking, heterogeneous interface, and other structural defects may prohibit layer-to-layer stacking[69]. Thus, different steric zippers presented in double-, triple-, and multiple-layer amyloid cross-seeding may explain a general structural polymorphism of amyloid seeding and cross-seeding, i.e., tightly interdigitating, dry steric zippers are general and strong building units for amyloid polymorphism, independent of complicated structural organizations with multiple layers. Due to the well-known lengthscale and timescale issues of MD simulations, it is computationally prohibitive to directly simulate the whole amyloid cross-seeding process starting from disordered monomers to highly β-structure-rich assemblies. Thus, we proposed another computational strategy to high-throughput examine the all possible cross-seeding interfaces between GNNQQNY and Aβ (or hIAPP) using in-house peptide-packing programs, followed by structural population analysis to computationally determine the most stable cross-seeding interfaces at the multiple low free energy states.

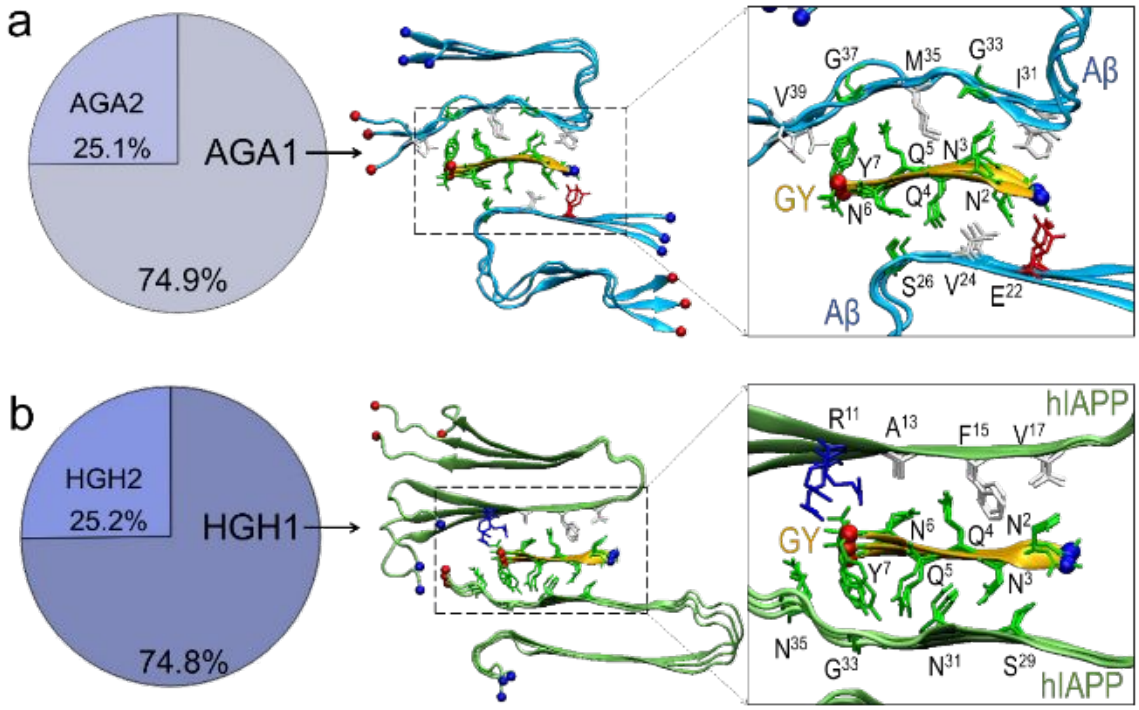

Figure 5. Highly populated and stable structures of triple-layer Aβ-GNNQQNY-Aβ and hIAPP-GNNQQNY-hIAPP assemblies. Structural populations and organization of different steric zippers in triple-layer **a** Aβ-GNNQQNY-Aβ and **b** hIAPP-GNNQQNY-hIAPP assemblies, with different orientations and contacting residues between two β-sheets from GNNQQNY and Aβ/hIAPP.

2.5. Disruption of steric zippers disfavors cross-seeding of GNNQQNY with Aβ and hIAPP

To test the important role of steric zippers in amyloid cross-seeding from a different aspect, we mutated Gln at a position 4 (Q4) of GNNQQNY with Ala and studied its homo-aggregation and co-aggregation with Aβ and hIAPP. As a result, Q4A mutant at all concentrates from 10 μM to even 1 mM completely lost its self-aggregation ability to form β-structure-rich amyloid-like fibrils (**Fig. 6b-c**). A number of our and other MD simulations also showed that Q4A mutation knocked down the intersheet steric zipper between two neighboring sheets, leading to the loss of sidechain-sidechain interactions and the destabilization of the whole assembly[51, 52, 70]. Further, co-incubation of non-amyloidogenic Q4A (15 μM) with either Aβ (15 μM) or hIAPP (15 μM) did not enable cross-seeding, instead exhibited similar aggregation kinetics to pure Aβ (**Fig. 6d**) or pure hIAPP (**Fig. 6e**). CD spectra in **Fig. 6f-g** confirmed that addition of equal molar of Q4A to Aβ or hIAPP did not largely alter their second structure changes. Particularly, Aβ-Q4A aggregates contained 56.1% of β-sheet structure (20.1% of parallel and 36.0% of antiparallel β-sheet structure), similar to 52.1% of β-sheet structure (31.7% of parallel and 20.4% of antiparallel β-sheet structure) in pure Aβ aggregates (**Fig. 6h**). Similarly, there was almost no influence of Q4A on the secondary structure change of hIAPP, as indicated by the respective 42.8% and 44.3% of β-sheet structure with and without Q4A (**Fig. 6i**).

In parallel, a series of MD simulations were performed to examine different

single-point mutations of GNNQQNY on the structural stability of double-layer GNNQQNY-Aβ and GNNQQNY-hIAPP assemblies. Distinct residue in GNNQQNY were selected and mutated to Ala in A5, A10, H9, and H13 cross-seeding assemblies (e.g., $A5^{N3A}$, $A5^{Q5A}$, $A5^{Y7A}$, $A10^{N2A}$, $A10^{Q4A}$, $H9^{N3A}$, $H9^{Q5A}$, $H9^{Y7A}$, $H13^{N2A}$, $H13^{Q4A}$ and $H13^{N6A}$) because these mutated residues were directly involved to form steric zippers with Aβ or hIAPP. As summarized in **Fig. S11**, all GNNQQNY mutants destabilized A5, A10, H9, and H13 assemblies to some extents, as indicated by the disruption of steric zippers (**Fig. S11a, b**), the decrease of β-sheet-to-β-sheet interactions (**Fig. S11c, f**), and the loss of β-structure (**Fig. S11d,g**) and hydrogen bonds (**Fig. S11e,h**), and even dissociation of double layers in $A10^{Q4A}$ and $H13^{Q5A}$ cases (**Fig. S11a, b**). Among these mutants, $A10^{Q4A}$ and $H13^{Q4A}$ assemblies had the same mutation residues of Q4A to experimental ones. It can be seen that $A10^{Q4A}$ assembly completely lost its interfacial steric zipper and double-layer organization, as indicated by the large separation of GNNAQNY from Aβ (**Fig. 6j**). While $H13^{Q4A}$ can still retain its double-layer association (**Fig. 6k**), inter-layer interactions to maintain steric zippers was reduced by 38% as compared to wild type H13 assembly. This destabilization is due not only to changes in sidechain interdigitation but also to the loss of 43% hydrogen bonds and 14% β-sheet structure. Thus, the destabilization of steric zippers by GNNQQNY mutants explains the loss of cross-seeding efficiency.

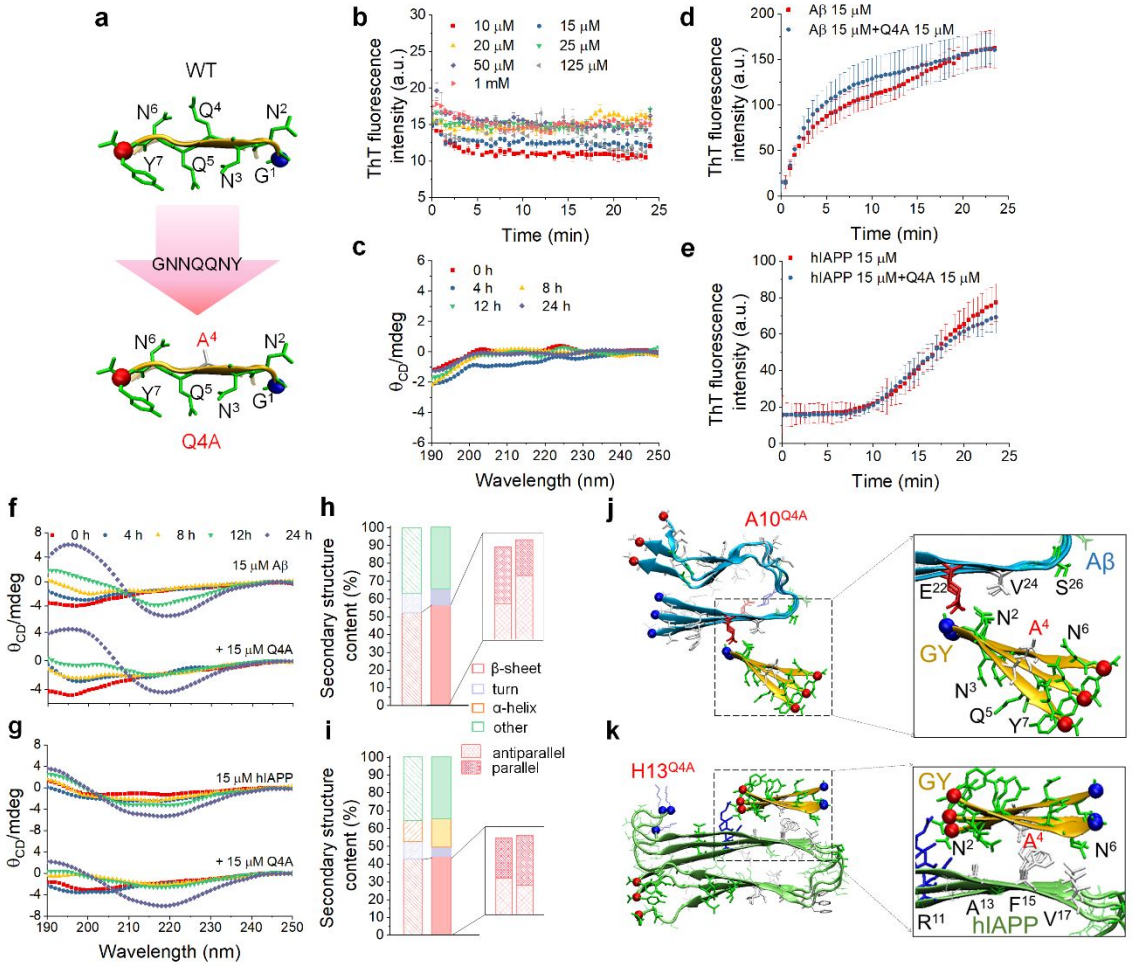

Figure 6. GNNQQNY mutant disfavors cross-seeding with Aβ and hIAPP. a Mutation of Gln residue of GNNQQNY at position 4 (Q4) to Ala (Q4A). **b** Time-dependent ThT fluorescence

curves of Q4A mutant at various concentrations of 10 μM -1 mM, confirming a non-amyloidogenic property. **c** Time-dependent CD spectra of 15 μM Q4A. Time-dependent ThT fluorescence curves to monitor the aggregation kinetics of **d** Aβ (15 μM) and **e** hIAPP (15 μM) with or without the addition of Q4A (15 μM). Time-dependent CD spectra of **f** Aβ (15 μM) and **g** hIAPP (15 μM) aggregating with or without Q4A (15 μM). Secondary structure distributions of **h** Aβ (15 μM) and **i** hIAPP (15 μM) with or without Q4A (15 μM) at 24 h. Inset: parallel and antiparallel β-sheet distributions. Molecular structures of mutants **j** Q4A-Aβ ($A10^{Q4A}$) and **k** Q4A-hIAPP ($H13^{Q4A}$), showing the disruption of steric zippers.

2.6. Cross-seeding of GNNQQNY with Aβ and hIAPP reduces cell toxicity

It is generally accepted that amyloid oligomers are more toxic than amyloid fibrils, thus they are considered as main species to cause cell death. Based on our cross-seeding results that GNNQQNY enables to promote both Aβ and hIAPP fibrillization by quickly converting oligomers into fibrils, we continued to investigate the cross-seeding effect of GNNQQNY with Aβ and hIAPP on cell toxicity using LDH and MTT assays, where cell toxicity and viability data were normalized by uncreated cell control group. As a control, GNNQQNY (15 μM) exhibited 14.3±1.2% apoptosis and 81.9±5.2% viability of SH-SY5Y cells (**Fig. 7 a-b**), as well as 3.2±1.3% apoptosis and 99.2±5.8% viability of RIN-m5F cells (**Fig. 7 c-d**), showing that GNNQQNY at this concentration was low cytotoxic to both cell lines within 48 h. The cross-seeding of GNNQQNY with Aβ at a 1:1 ratio for 48 h reduced cell apoptosis to 24.4±0.5% (**Fig. 7a**) and increased cell viability to 75.0±5.9% (**Fig. 7b**), as compared to Aβ-induced cell apoptosis of 31.7±3.0% and cell viability of 40.6±3.1%. Consistently, the cross-seeding of GNNQQNY with hIAPP slightly improved the cell apoptosis of 17.8±1.0% and cell viability of 38.2±2.8%, as compared to hIAPP-induced cell apoptosis of 22.0±0.9% and cell viability of 30.0±3.2% (**Fig. 7c-d**). GNNQQNY appears to exert the less cell protection effect from hIAPP-induced cell toxicity than Aβ-induced cell toxicity, probably because the slower aggregation of hIAPP makes GNNQQNY less efficient to convert highly toxic oligomers into less toxic fibrils[71, 72], consistent with ThT and SDS-page results.

To better understand the origin of the reduced cell toxicity by amyloid cross-seeding, we performed carboxyfluorescein entrapped large unilamellar vesicles (LUVs, consisting of DOPC:DOPS liposomes) leakage assay to monitor cross-seeding-induced membrane disruption. Untreated LUVs were used as a reference for spontaneous leakage of the dye and were compared to LUVs incubated with pure amyloid aggregates or amyloid cross-seeding aggregates. **Fig. 6e** showed that freshly prepared Aβ (15 μM) caused rapid leakage of dye (43.8±0.9% leakage) in 7.5 h, after which dye release was saturated, indicating that Aβ disrupts the lipid bilayer during its aggregation. Addition of GNNQQNY to Aβ caused the slower and less leakage (35.4±2.1% leakage). The time of dye leakage is similar to that of accelerating growth in ThT results (**Fig. 1a**), indicating that a partial blockage of membrane disruption by cross-seeding is attributed to the bypass of the formation of toxic Aβ oligomers at lag phase. In contrast, LUVs with and without GNNQQNY caused the almost same dye leakage kinetics and final dye-leakage intensity of ~47%, indicating that presence of GNNQQNY has little influence on hIAPP-induced membrane leakage, consistent with ThT kinetics data that the lag phase remained unchanged in the presence and absence of GNNQQNY (**Fig. 2a**). These results confirm

that amyloid oligomers in lag or early growth phases cause more membrane disruption, and the reduction in membrane disruption is determined by the extent of the conversion of amyloid oligomers by GNNQQNY via its cross-seeding effect.

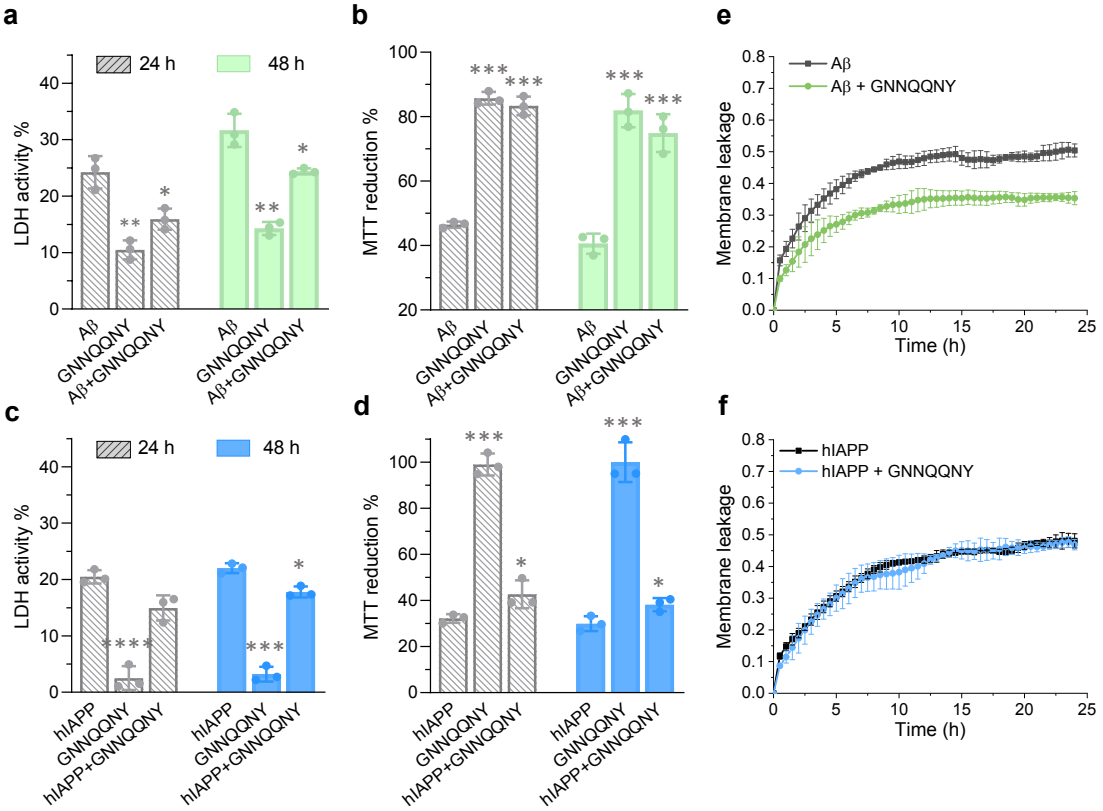

Figure 7. GNNQQNY reduces the amyloid oligomer-induced cell toxicity. a, b Aβ-induced (15 μM) SH-SY5Y cell toxicity and **c, d** hIAPP-induced (15 μM) RIN-m5F cell toxicity, as evaluated by (**a, c**) LDH activity assay and (**b, d**) MTT reduction assay in the absence and presence of GNNQQNY (15 μM). Statistical significance from the control (cell treated with Aβ/hIAPP alone) was analyzed by one-way ANOVA test and t-test. (*P < 0.05, **P < 0.01, ***P < 0.001, three biological repeats n = 3). Standard membrane leakage assay for quantifying **e** 15 μM Aβ- and **f** 15 μM hIAPP-induced membrane damage with and without 15 μM GNNQQNY. Data shown are mean ± s.d. of three-independent experiments (n=3). The time-dependent membrane leakage in the presence of Aβ/hIAPP or Aβ/hIAPP+GNNQQNY was analyzed by two-way ANOVA. Comparison of membrane leakage between Aβ and Aβ+GNNQQNY samples reveals P value < 0.01.

3. Discussion

Amyloid cross-seeding is, despite still under investigation, considered as one of main mechanisms for the spread of the overlapping pathologies across different cells and tissues between different PMDs and epidemics[73-75]. Epidemiological studies have pointed a statistic connection between prion disease (PD), Alzheimer disease (AD), and type II diabetes (T2D), as evidenced by (i) the co-occurrence of different amyloid diseases in the same individuals and (ii) the increased risk of developing the other two diseases if any abovementioned disease is presented. Such amyloid-linked pathologies between PD, AD, and T2D suggest the possible cross-seeding between the disease-related specific proteins to produce heterogenous amyloid aggregates, which may transport to heart, liver, and even

intestine via spinal fluid and blood plasma to achieve amyloid transmission[76, 77].

From a viewpoint of protein misfolding and protein-protein interaction, considering the conformational complexity and polymorphism of amyloid proteins, whenever co-assembly of any two amyloid proteins, each type of amyloid proteins generates a vast number of structural ensembles with different populations at transient states. In principle, such structural diversity and instability between and within both amyloid aggregates will create high cross-species barriers to prevent their interactions and co-assembly into highly structured aggregates. Thus, to make cross-seeding happen, it is a necessary but not sufficient condition to acquire some structural compatibility between two amyloid aggregates. Specifically, highly similar β-sheet structures in different amyloid aggregates allow to largely lower the cross-seeding barriers and acts as general structural motifs and interaction template for amyloid cross-seeding. However, not any two β-sheets from different amyloid aggregates necessarily enable cross-seeding interactions, depending on both local conformational compatibility and populations of β-sheet structures between different amyloid aggregates from different aggregation pathways.

To line with the amyloid cross-seeding hypothesis above, we are the first to study the cross-seeding between GNNQQNY associated PD, Aβ associated with AD, and hIAPP associated with T2D using experiments and simulations, as well as propose the conformational fitting and selective binding to explain the cross-seeding of GNNQQNY with Aβ and hIAPP. First, collective results from ThT, AFM, and CD demonstrate that on one hand, GNNQQNY indeed cross-seeds with both Aβ and hIAPP to promote their structural conversion towards β-sheet structures by 34.5-57.0% (**Fig. 1g & 2g**) and amyloid fibrillization up to 142-200% (**Fig. 1b & 2b**), suggesting that a general mechanism governs their cross-seeding behavior. Molecular simulations further confirm that GNNQQNY can laterally and tightly associate with Aβ and hIAPP via β-sheet interactions to form a variety of GNNQQNY-Aβ and GNNQQNY-hIAPP complexes in double-layer and triple-layer organizations, which reflect a general and intrinsic nature of amyloid polymorphism. While all of stable cross-seeding complexes display different β-sheet organizations, they all form different steric zippers at their interfaces, whose side chains of two β-sheets of different amyloid aggregates are geometric complementarity to form a dry interface, rendering the two β-sheets from different amyloid aggregates to pack more closely. Beyond double-layer cross-seeding structures stabilized by a single steric zipper, a combination of two different steric zippers enables to form multiple, stable triple-layer cross-seeding complexes. Theoretically, the co-existence of both double- and triple-layer cross-seeding complexes, associated by single or two steric zippers, allows to cover all possible multiple β-sheet-layer packing via steric zippers, revealing that (i) steric zipper could be a basic structural unit to enable the cross-seeding of GNNQQNY with Aβ and hIAPP, explaining its promotion effect on amyloid fibrillization, and (ii) different steric zippers in cross-seeding aggregates are compatible with slow fibril nucleation and faster fibril growth, explaining amyloid polymorphism.

On the other hand, cross-seeding efficiency of GNNQQNY-Aβ and

GNNQQNY-hIAPP is also varied with different sequences, concentrations, and preformed seeds of Aβ and hIAPP, indicating the existence of cross-species barriers along the folding pathways of different amyloid proteins. Cross-seeding results suggest two co-aggregation pathways via conformational-selection model and template-assisted growth model, largely depending on the target amyloid protein aggregation states and conformation populations (**Fig. 8**). We found that the cross-seeding of GNNQQNY with Aβ/hIAPP monomers or small oligomers at the early aggregation stage is more efficient than that of GNNQQNY with large Aβ/hIAPP (proto)fibrils and that of homo-seeding of either Aβ or hIAPP. In the cases of GNNQQNY cross-seeding with early Aβ/hIAPP oligomers, conformational-selection model (**Fig. 8a**) suggests that as compared to Aβ-Aβ or hIAPP-hIAPP homo-seeding, GNNQQNY is much easier to adjust its conformations to accommodate with small Aβ/hIAPP oligomers due to very small structural ensemble spaces. Small GNNQQNY-Aβ/hIAPP seeds will be further associated together to grow into higher-order aggregates. This model explains the observation that addition of GNNQQNY to early Aβ/hIAPP aggregates rapidly promotes their aggregation kinetics (**Fig. 1a** & **2a**). Differently, when adding GNNQQNY to Aβ/hIAPP seeds at the growth phases, Aβ/hIAPP aggregates serve as structural templates to recruit GNNQQNY monomers in a less efficient way (**Fig. 8b**). Considering the non-amyloidogenic nature of GNNQQNY at 15 μM, it is more challenging for Aβ/hIAPP seeds to simultaneously recruit multiple GNNQQNY molecules at a time to form heterogeneous steric-zipper nucleus. This explanation is further supported by the loss of cross-seeding ability when adding GNNQQNY to Aβ/hIAPP protofibrils (**Fig. 3a, b**). Additional energy barrier is imposed for hydrophilic, soluble GNNQQNY to interact with more hydrophobic, less-soluble Aβ/hIAPP protofibrils. Both models apparently consider the existence of cross-seeding barriers and follow selective co-assembly of conformational compatible amyloid species of different sequences for the onset and efficiency of amyloid cross-seeding.

Generally speaking, *in vitro/in silico* studies of amyloid peptides are usually performed under dilute conditions, in sharp contrast to *in vivo* environment that is much more complex and involve a large number of different biomolecules such as proteins, nucleic acids, lipids, and metabolites. These biomolecules occupy a significant fraction (~25%) of cellular volume and the extracellular matrix (e.g., 10% of blood plasma), leading to the crowded cell environment[78, 79]. The molecular crowding effect *in vivo* will influence the excluded volume and solution viscosity, both of which affect amyloid aggregation. It is worthy to note that while our *in vitro* and *in silico* study may not be able to completely mimic the *in vivo* cross-seeding process, it also provides the first fundamental understanding of amyloid cross-seeding at both protein and cellular levels.

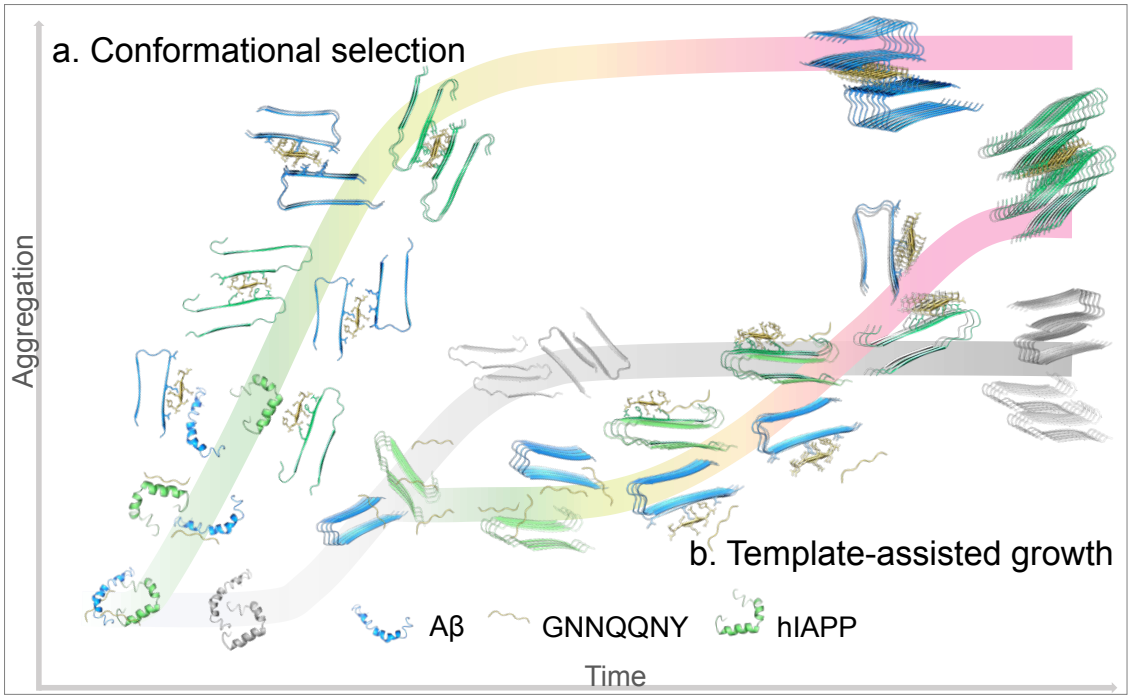

Figure 8. Mechanistic models for GNNQQNY cross-seeding with Aβ and hIAPP at different aggregation states. a GNNQQNY cross-seeds with small Aβ/hIAPP monomers or oligomers through a conformational-selection pathway, in which short GNNQQNY preferentially accommodate its conformations with Aβ/hIAPP to form into high-order aggregates. **b** GNNQQNY cross-seeds with large Aβ/hIAPP aggregates or protofibrils through a template-assisted growth pathway, in which the preformed Aβ/hIAPP aggregates recruit GNNQQNY molecules slowly to form heterogeneous aggregates.

In summary, this work demonstrates, for the first time, the dual cross-seeding ability of GNNQQNY to facilitate both Aβ and hIAPP fibrillization, which may explain molecular crosstalk between PD, AD, and T2D as a result of amyloid cross-seeding between their corresponding disease-causative peptides. Collective experimental and simulation data reveal that (1) steric β-zippers, formed by a pair of tightly interdigitated β-sheets of different amyloid peptides, serve as a general interactive and structural unit to initiate and promote amyloid cross-seeding via conformational fitting and selective binding mechanism. (2) Different steric β-zippers alone or in combination present different packing structures and aggregation pathways to form a variety of cross-seeding assemblies, enriching amyloid polymorphism. (3) Single-point Q4 mutation of GNNQQNY disrupt the steric zipper formation and thus reduces its cross-seeding ability to interact with Aβ and hIAPP, again highlighting the importance of steric β-zippers in amyloid cross-seeding. (4) Different binding affinities of GNNQQNY to Aβ and hIAPP seeds at different aggregation stages demonstrates the existence of cross-seeding barriers that govern steric β-zipper formation and cross-seeding efficiency.

4. Methods

Preparation of Amyloid Monomers

Synthetic peptides (≥ 95%) without terminal modifications, including GNNQQNY, $A\beta_{42}$, and $hIAPP_{37}$ were purchased from AnaSpec (CA, USA), and single-point mutant GNNAQNY (Q4A) from GenScript (NJ, USA). All the bulk powdered peptides were dissolved in 1,1,1,3,3,3-hexafluoro-2-propanol (HFIP, ≥ 99.9%) and incubated at ambient temperature for 2 h to breakdown pre-existing aggregates. Solutions of monomeric peptides were prepared by sonication in ice bath and subsequently centrifugation at 14000 rpm, 4 °C for 30 min. The monomeric peptides were extracted after lyophilizing the supernatant, and stored under −20°C. For preparation of monomeric peptide stocks, dried peptide films were solubilized in 10 mM NaOH, and diluted into 10 mM phosphate-buffered saline (PBS), pH 7.4, stored on ice for subsequent usage within 1 hour.

Thioflavin T (ThT) Fluorescence Assay

ThT fluorescence was monitored by using the kinetic bottom-read mode of a SpectraMax M3 microplate reader (Molecular Devices, CA, USA) with excitation at 450 nm and emission at the range of 470 nm to 500 nm. Samples were prepared on ice by dissolving the $A\beta_{42}$ and $hIAPP_{37}$ peptides (15 or 30 μM) in the absence or presence of GNNQQNY (15 μM) in 10 μM ThT-Tris buffer solution. The ThT fluorescence measurement was conducted in triplicate per sample. After transferring the samples to 96-well plate in the plate reader, the aggregation was initiated at 37 °C, and fluorescence intensity data were recorded consistently at 30 min intervals for 24 h.

Atomic Force Microscopy (AFM)

During the aggregation process, the morphology changes of peptides were imaged by using Nanoscope III multimode AFM (Veeco, NY, USA). The amyloid peptides were incubated in 10 mM PBS buffer, pH 7.4 with or without GNNQQNY at 37 °C, and at different time intervals samples (20 μL) were deposited on mica for 2 min at ambient temperature. The mica substrate was washed with deionized water to get rid of salts and dried by gentle airflow before stored in sealed containers. The imaging was carried out in tapping mode with a scan rate of 1.0 Hz, and silicon AFM probe with a nominal radius of < 10 nm and 300 kHz resonant frequency (Aspire, USA).

In the present experiments, the measurement of each sample was conducted at a minimum force between the tip and sample, and therefore does not strongly influence the morphology of the observed object. Additionally, the geometry of tip does not strongly affect the measurement of the cross-sectional height of observed objects. However, a tip with an apical radius of equal or larger than the dimensions of the object will affect the lateral resolution due to convolution effect, resulting in artifacts arising on lateral dimensions[78]. Here, objects with typical lateral dimensions within 10 nm were measured by a tip with < 10 nm radius, thus we quantified the deconvoluted width of the aggregates,

and compare the morphology of different samples consistently. Images were flattened and analyzed by Nanoscope software.

Circular Dichroism (CD) Spectroscopy

The secondary structure of protein can be monitored by far-UV CD spectroscopy with a J-1500 spectropolarimeter (Jasco Inc., Japan). In all, 15 μM $A\beta_{42}$ or $hIAPP_{37}$ were incubated at 37 °C in 10 mM phosphate-buffered saline (PBS, pH 7.4) in the presence or absence of 15 μM GNNQQNY. 150 μL of samples were pipetted into a 1 mm optical path length CD cuvette, and the spectra were scanned between 190 and 250 nm with a step size of 0.5 nm and 50 nm/min scan rate, in all CD measurements after each time interval. The spectra were analyzed after subtracting the background signal of pure PBS buffer, and averaged by triplicated scan per sample. The secondary structural contents were determined by using the Beta Structure Selection (BeStSel) algorithm[79] (http://bestsel.elte.hu/).

Sodium Dodecyl Sulfate–Polyacrylamide Gel Electrophoresis (SDS-PAGE)

The aggregation process of 15 μM $A\beta_{42}$ or $hIAPP_{37}$ in the absence or presence of 15 μM GNNQQNY were assessed by SDS-PAGE. Freshly isolated amyloid solutions from aggregation experiments at different aggregation time were immediately subjected to photo-induced crosslinking of unmodified proteins (PICUP) and analyzed by SDS-PAGE. An equal volume mixture of sample and 2× laemmli sample buffer (2.1% SDS, 26.3% w/v glycerol, 0.01% bromophenol blue, 65.8 mM Tris-HCl buffer pH 6.8) was electrophoresed in 8% Bis-Tris SDS-PAGE gels. Gels were run at 80 V in MES SDS buffer and subsequently visualized by silver staining.

Surface Plasmon Resonance (SPR) Spectroscopy

The binding analysis was performed using a custom-built four-channel SPR instrument at ambient temperature. A dextran-modified SPR sensor chip was prepared following the well-established method[80]. Briefly, the dextran-modified SPR sensor chip was prepared by immersing the gold chip in a 5 mM 11-mercapto-1-undecanol in ethanol/water (8:2) solution for 24 h, reacted with epichlorohydrin (2% v/v) in 0.1 M NaOH for 3 h, , and transferred to a 300 g/L dextran solution (500 kDa) in 0.1 M NaOH for 24 h. The resultant surfaces were washed with Milli-Q water and subsequently immersed in 1.0 M bromoacetic acid in 2 M NaOH for 24 h to achieve the dextran-modified SPR sensor chip.

For GNNQQNY immobilization, the SPR sensor chip was activated by an equimolar mix of NHS (N-hydroxysuccinimide) and EDC (N-ethyl-N-(diethylaminopropyl) carbodiimide) and coupled with GNNQQNY in acetic acid buffer (10 mM, pH 4.5), followed by blocking with ethanolamine (**Fig. S5a**). The final coupling level of GNNQQNY was kept constant around 8 resonance units (1 RU=1500 ng protein/mm^2). The interaction of GNNQQNY with $A\beta_{42}$ or $hIAPP_{37}$ was performed by injecting a serial diluted $A\beta_{42}$ or $hIAPP_{37}$ (1−15 μM) in running buffer (10 mM PBS and 0.005 wt% tween-20, pH 7.4) over channels at a flow rate of 30 μL/min. Dissociation constant (K_D) values were evaluated using Anabel software[81] (http://anabel.skscience.org/) by fitting the

data using a 1:1 Langmuir binding model (**Fig. S5b**) and observed binding constant (k_{obs}) linearization method.

Cell Cultures

Human SH-SY5Y neuroblastoma cells (ATCC® CRL-2266™, VA, USA) were cultured in sterile-filtered Eagle's minimum essential medium (EMEM) and Ham's F-12 medium (1:1) supplemented with 10% fetal bovine serum (FBS) and 1% penicillin/streptomycin. Rat insulinoma cells RIN-m5F (ATCC® CRL-11605™, VA, USA) were incubated in sterile-filtered RPMI-1640 medium mixed with 10% FBS and 1% penicillin/streptomycin. Cell cultures were maintained in a 5% CO_2 humidified incubator at 37 °C to reach 80% confluence.

MTT Reduction Assay

The cell viability was determined by well-established 3-(4,5-dimethylthiazole-2-yl)-2,5-diphenyltetrazolium bromide (MTT) reduction assay. SH-SY5Y or RIN-m5F cells were seeded in 96-well plate at 10^4 cells per well density for 12 h. 15 μM $A\beta_{42}$ or $hIAPP_{37}$ monomer was added and incubated with or without equal molar concentrations of GNNQQNY to cell culture medium. After 24 h or 48 h, cells were labelled in 0.5 mg/mL MTT culture medium solution at 37 °C for 4 h, and dissolved the formazan crystals in dimethyl sulfoxide. The absorbance value was read at 540 nm, and the cell viability was determined as the percentage of MTT reduction as compared to untreated cells.

Lactate Dehydrogenase (LDH) Activity Assay

The cytotoxicity of amyloid peptides was assessed by LDH activity. Cytosolic enzyme LDH will be released into cell culture media after the plasma membrane is damaged, which can be measured as biomarker to quantify the cytotoxicity. Spontaneous LDH release was measured as positive control in untreated cells, and a total LDH release was measured by cell lysis as negative control in Lysis Buffer (10×). 15 μM $A\beta_{42}$ or $hIAPP_{37}$ monomer was added in the presence or absence of equal molar GNNQQNY and added to the culture medium of 10^4 density cells seeded in 96-well plates for 24 h. The leaked LDH activity in the medium was evaluated by the Pierce™ LDH Cytotoxicity Assay Kit (Thermo, USA), and the absorbance was read at the wavelength of 490 nm and 680 nm by the microplate reader. The LDH activity values were normalized to spontaneous LDH release, and cytotoxicity values were calculated in percentages of total LDH release.

Large Unilamellar Vesicles (LUVs)

The liposomes vesicles composed of zwitterionic phosphatidylcholine DOPC and anionic phosphatidylserine DOPS at a molar ratio of 7:3 have been widely used as an intra-cellular membrane model for different biological purposes of cell leakage, drug/gene carriers, and ion/protein diffusion[82-84]. Both DOPC and DOPS have two mono-unsaturated chains with an inverted cone lipid shape and the smaller hydrophobic thickness, all of which are amenable to the preparation of the stable and curved vesicles[85]. To prepare the liposomes vesicles, DOPC and DOPS were dissolved in chloroform and mixed in 7:3 molar ratio.

After evaporating the mixture under nitrogen airflow and further dried in high vacuum for at least 30 min, the lipid film was obtained. The lipid film was then hydrated in Tris buffer (10 mM Tris-HCl, 100 mM NaCl, pH 7.4) for 1 h to reach a concentration of 10 mM. The lipid solution was then subjected to 10 freeze-thaw cycles and extruded 10 times through a 200 nm pore size filters to obtain a uniform LUVs size.

For the membrane leakage experiment, LUVs containing 5(6)-carboxyfluorescein were prepared similarly except the lipid film was hydrated with saturated 5(6)-carboxyfluorescein in Tris buffer. The free 5(6)-carboxyfluorescein was removed from the 5(6)-carboxyfluorescein-filled LUVs using a PD 10 desalting column (GE Healthcare Life Science) by carefully eluting with Tris buffer (10 mM Tris-HCl, 100 mM NaCl, pH 7.4). Dynamic light scattering was used to ensure the proper diameter and polydispersity and the vesicle solution should be used right after being prepared.

Membrane Permeability Assays

The leakage experiment was conducted to evaluate the amyloid peptide affiliation and induced damage to the membrane. The 5(6)-carboxyfluorescein encapsulated LUVs were used to mimic cell membranes for tracking the membrane disruption induced by amyloid kinetically. 15 μM $A\beta_{42}$ or $hIAPP_{37}$ monomer was added in the presence or absence of equimolar GNNQQNY to 10 mM 5(6)-carboxyfluorescein encapsulated LUVs (10 mM Tris·HCl, 100 mM NaCl, pH 7.4) solution, and incubated in 37 °C. The 5(6)-carboxyfluorescein fluorescence signal was continuously measured at excitation and emission wavelength of 485 nm and 535 nm. A maximum leakage should be determined by adding Triton X-100 to a final concentration of 0.1% (v/v) to disrupt membranes thoroughly. The membrane permeability was determined as percentage fluorescence change $L(t) = (F_t - F_0)/(F_{100} - F_0)$, where L(t) represent the normalized membrane leakage, F_t is the measured fluorescence intensity at time t, F_0 is the initial fluorescence intensity at times t = 0 and F_{100} is the intensity after addition of Triton X-100.

Molecular Simulations of Amyloid Cross-seeding

Given that no atomic structural models are currently available to describe the cross-seeding complexes of GNNQQNY-Aβ and GNNQQNY-hIAPP, we developed a computational platform combining in-house peptide-packing program and all-atom molecular dynamics (MD) simulations to systematically screen and determine the most possible cross-seeding structures of GNNQQNY-Aβ and GNNQQNY-hIAPP aggregates with steric zippers in double-layer and triple-layer organizations and to reveal the underlying forces to drive the amyloid cross-seeding between GNNQQNY, Aβ, and hIAPP via three steps.

Step 1: Interfacial scanning and packing for amyloid cross-seeding aggregates. An in-house peptide-packing program was developed to systematically search and determine all possible the lateral β-layer-to-β-layer interfacial packing between GNNQQNY and Aβ (or hIAPP) oligomers at the low energy minimization states. As shown in **Fig. S6-7**, four key parameters were considered for coarsely identifying the low-energy amyloid

cross-seeding packings, including (1) interlayer translation along the *x* axis (d_x, one layer was translated with respect to another layer along the β-strand direction), (2) interlayer distance between two amyloid oligomers along the *y* axis (d_y, along lateral direction), (3) layer-to-layer orientations (parallel vs. antiparallel), and (4) interfacial sidechain contacts of GNNQQNNY (even face vs. odd face of GNNQQNY) relative to Aβ or hIAPP oligomers. Four typical families of cross-seeding interfaces were constructed based on a given orientation between GNNQQNY and target oligomers (Aβ or hIAPP) and specific sidechains of GNNQQNY facing towards target oligomers (Aβ or hIAPP: $[^{GY}O\text{-}C^{A\beta}]_{\uparrow\uparrow}$, $[^{GY}O\text{-}N^{A\beta}]_{\uparrow\downarrow}$, $[^{GY}E\text{-}C^{A\beta}]_{\uparrow\downarrow}$, $[^{GY}E\text{-}N^{A\beta}]_{\uparrow\downarrow}$ and $[^{GY}O\text{-}C^{hP}]_{\uparrow\uparrow}$, $[^{GY}O\text{-}N^{hP}]_{\uparrow\downarrow}$, $[^{GY}E\text{-}C^{hP}]_{\uparrow\downarrow}$, $[GY^{E}\text{-}^{N}hP]_{\uparrow\downarrow}$, where the first and last letters of full name of amyloid peptides were used as the corresponding abbreviations (i.e., GY=GNNQQNY, Aβ=Aβ, and hP=hIAPP); the letters "O" and "E" of GNNQQNY represent the odd face containing G1, N3, Q5, Y7 residues in odd positions and even face containing N2, Q4, N6 residues in even positions, respectively; the letters of "N" and "C" of both Aβ and hIAPP represent N-terminal and C-terminal β-sheet regions, respectively; and the symbols of "↑↑" and "↑↓" represent parallel and antiparallel orientation between the two β-sheets of GNNQQNY and Aβ, respectively. Specifically, a structural ensemble of any given cross-seeding interface will be generated by varying interlayer distance (d_y) of every ~1 Å between the two amyloid oligomers and interlayer translation along the *x* axis (d_x) of every ~1 Å. Thus, a specific ensemble of amyloid cross-crossing interface contains a total of 4,640 cross-seeding structures, each of which was minimized and compared in energy to determine their low-energy cross-seeding structures. As a result, 11 of 2,240 GNNQQNY-Aβ (A1-A11 in **Fig. S6**) and 14 of 2,400 GNNQQNY-hIAPP cross-seeding interfaces (H1-H14 in **Fig. S7**) were identified and selected at their low energy states, all of which adopted double-layer associations with different steric zippers formed by different β-sheet packings and orientations at cross-seeding interfaces. It should be noted that the low-energy structures determined by energy minimization method do not necessarily imply the most stable structures in the explicit solvent due to the lack of explicit peptide-water interactions, thus all of 25 double-layer cross-seeding models were further examined for their structural stability by subsequent all-atom explicit-solvent MD simulations.

Step 2: Stable steric zippers from double-layer cross-seeding models. Next, a total of 11 GNNQQNY-Aβ and 14 GNNQQNY-hIAPP cross-seedings were solvated in in a TIP3P water box with a margin of at least 15 Å from any edge of the water box to any peptide atom. Any water molecule within 2.4 Å of the peptide was removed. Each system was then neutralized by adding Cl¬- and Na+ ions to mimic ~150 mM ionic strength. Then, these GNNQQNY-Aβ and GNNQQNY-hIAPP cross-seedings were subject to all-atom MD simulations in explicit water for determining stable steric zippers. As shown in **Table S1**, after a total of 1,250 ns simulations (50 ns for each system), 5 of 11 GNNQQNY-Aβ and 8 of 14 GNNQQNY-hIAPP were found to be structurally stable, with well-reversed steric zippers at interface, β-layer association, and overall structural integrity. Stable double-layer steric zippers will be further served as basic building blocks to construct triple-layer cross-seeding models and to reveal the GNNQQNY-promoted cross-seeding behavior at atomic details.

Step 3: Stable Triple-layer cross-seeding models. Given that stable double-layer steric zippers with distinct interfaces are determined by MD simulations in Step 2, a combination of two possible steric zippers is able to exclusively construct sandwich-like, triple-layer, cross-seeding models, in which GNNQQNY oligomers were placed in between Aβ (or hIAPP) oligomers with the two exact steric zipper interfaces (i.e., the same orientation, position, and sidechain contacts) as determined in Step 2. As a result, three-layer models of Aβ-GNNQQNY-Aβ and hIAPP-GNNQQNY-hIAPP were constructed by considering different combinations of two steric zipper interfaces. Further 100-ns MD simulations demonstrated that all triple-layer cross-seeding models were structurally stable, with well-reversed overall structural integrity without any tendency of disassociation, as well as well-interdigitated steric zippers at interface. All double-layer and triple-layer cross-seeding models were summarized in the **Table S1**.

Amyloid Models. Pentamers were selected as basic building units to study the structure, dynamics, and interactions of amyloid cross-seeding between them. The $A\beta_{17-42}$ structure (PDB: 2BEG) was taken from the ssNMR and H/D exchange model as determined by the Riek lab[59]. While the first 1-16 sequence is disordered and has less tendency to form fibrils, it functions as membrane-binding motifs. In our simulations, we mainly focus on Aβ fibril structures, not Aβ-membrane interactions, thus $A\beta_{17-42}$ model was selected for our cross-seeding study. Initial monomeric structures of GNNQQNY (PDB: 1YJP)[86], $A\beta_{17-42}$ (PDB: 2BEG)[59], and $hIAPP_{37}$[60] structures were obtained from the solid-state NMR and x-ray crystal fibrillar structures. For three pentamer models, they were constructed by stacking five monomers on top of each other with initial interpeptide separation of ~4.7 Å in an in-register manner. All GNNQQNY, $A\beta_{42}$, and $hIAPP_{37}$ pentamers adopted well-preserved β-sheet structure. The N- and C-termini of all peptides were capped by NH_3+ and COO- groups, respectively. For GNNQQNY mutant systems, single-point Ala mutation was used to replace those residues involving in the formation of cross-seeding steric zippers.

MD Simulations. All MD simulations were performed using the NAMD software[87] with CHARMM27 force field for peptides and TIP3P for water[88]. MD simulations were performed using an isothermal-isochoric ensemble (NPT, T=310K and P=1 atm) under periodic boundary conditions with the minimum image convention. The Langevin piston method with a decay period of 100 fs and a damping time of 50 fs was used to maintain a constant pressure of 1 atm, while the Langevin thermostat method with a damping coefficient of 1 ps^{-1} was used to control the temperature at 310 K. All covalent bonds involving hydrogen were constrained so that 2-fs timestep was used in the velocity Verlet integration. Van der Waals (VDW) interactions were calculated by the switch function with a twin-range cutoff. Long-range electrostatic interactions were calculated using the force-shifted method with a 14 Å cutoff. Each modeled system was run twice with the same initial coordinates but different initial velocities to verify statistical accuracy. All analyses were performed using tools within the CHARMM, VMD[89], and in-house FORTRAN.

Cross-Seeding Population Analysis. To identify the most populated cross-seeding assemblies in the complex energy landscape, we extracted 1000 structures from the last 10-ns MD simulation trajectories of double-layer GNNQQNY-Aβ (A1, A3, A4, A5, and A10), double-layer GNNQQNY-hIAPP (H1, H2, H3, H4, H7, H8, H9, and H13), GNNQQNY-Aβ-GNNQQNY (AGA1 and AGA2), and GNNQQNY-hIAPP-GNNQQNY (HGH1 and HGH2) assemblies after removing water molecules and counter ions. For any given cross-seeding assembly model, $1000 \times 4 = 4000$ conformers were produced and then used to produce the energy landscape of each cross-seeding assembly for determining the population probability of conformers using an in-house Monte Carlo program. To reduce the effect of thermal fluctuations by MD simulations, 400-step ABNR energy minimizations were applied to all conformers of each cross-seeding assembly. Next, conformation energies of these conformers were computed using generalized Born method with molecular volume (GBMV), consequently producing a Markov energy chain [E_1, E_2, ..., E_i, ..., E_n] for all conformers. To obtain the most populated conformers, conformational energies were calculated for two selected structures of conformers i and j based on the GBMV model. Further, transition probabilities (e.g. acceptance probability) from conformer i to conformer j were calculated based on the function of $P_{accept,\ move} = \min[1, \exp((E_i - E_j)/kBT)]$ using metropolis algorithm. As a result, the number of "accepted" structures (N_i) for any conformer i was quantified from 1 million samplings. The relative populated conformer i with relative larger $p_i = N_i/N_{total}$ was determined from the energy landscape.

Acknowledgment. J.Z. thanks financial supports, in partial, from previous NSF (CBET-1510099, DMR-1806138, and CMMI-1825122).

References

1. F. Chiti and C. M. Dobson, *Annual Review of Biochemistry*, 2017, **86**, 27-68.
2. C. Soto, *Nature Reviews Neuroscience*, 2003, **4**, 49-60.
3. F. Chiti and C. M. Dobson, *Annual Review of Biochemistry*, 2006, **75**, 333-366.
4. R. P. R. Nanga, J. R. Brender, S. Vivekanandan and A. Ramamoorthy, *Biochimica et Biophysica Acta (BBA) - Biomembranes*, 2011, **1808**, 2337-2342.
5. R. P. R. Nanga, J. R. Brender, J. Xu, K. Hartman, V. Subramanian and A. Ramamoorthy, *Journal of the American Chemical Society*, 2009, **131**, 8252-8261.
6. S. Vivekanandan, J. R. Brender, S. Y. Lee and A. Ramamoorthy, *Biochemical and Biophysical Research Communications*, 2011, **411**, 312-316.
7. P. K. Mandal, J. W. Pettegrew, E. Masliah, R. L. Hamilton and R. Mandal, *Neurochemical Research*, 2006, **31**, 1153-1162.
8. I. C. Stancu, B. Vasconcelos, D. Terwel and I. Dewachter, *Molecular Neurodegeneration*, 2014, **9**, 1-14.
9. X. Li, X. Zhang, A. R. A. Ladiwala, D. Du, J. K. Yadav, P. M. Tessier, P. E. Wright, J. W. Kelly and J. N. Buxbaum, *Journal of Neuroscience*, 2013, **33**, 19423-19433.
10. P. Liu, S. Zhang, M. S. Chen, Q. Liu, C. Wang, C. Wang, Y. M. Li, F. Besenbacher and M. Dong, *Chemical communications*, 2012, **48**, 191-193.
11. B. O'Nuallain, A. D. Williams, P. Westermark and R. Wetzel, *Journal of Biological Chemistry*, 2004, **279**, 17490-17499.
12. K. C. Luk, D. J. Covell, V. M. Kehm, B. Zhang, I. Y. Song, M. D. Byrne, R. M. Pitkin, S. C. Decker, J. Q. Trojanowski and V. M. Y. Lee, *Cell Reports*, 2016, **16**, 3373-3387.
13. K. Ono, R. Takahashi, T. Ikeda and M. Yamada, *Journal of neurochemistry*, 2012, **122**, 883-890.
14. M. R. Krebs, L. A. Morozova-Roche, K. Daniel, C. V. Robinson and C. M. Dobson, *Protein science : a publication of the Protein Society*, 2004, **13**, 1933-1938.
15. R. Morales, K. M. Green and C. Soto, *CNS & neurological disorders drug targets*, 2009, **8**, 363-371.
16. Y. Atsmon-Raz and Y. Miller, *ACS chemical neuroscience*, 2016, **7**, 46-55.
17. K. C. Luk, V. Kehm, J. Carroll, B. Zhang, P. O'Brien, J. Q. Trojanowski and V. M.-Y. Lee, *Science*, 2012, **338**, 949-953.
18. R. Hu, M. Zhang, H. Chen, B. Jiang and J. Zheng, *ACS Chemical Neuroscience*, 2015, **6**, 1759-1768.
19. B. Ren, Y. Zhang, M. Zhang, Y. Liu, D. Zhang, X. Gong, Z. Feng, J. Tang, Y. Chang and J. Zheng, *Journal of Materials Chemistry B*, 2019, **7**, 7267-7282.
20. R. Hu, B. Ren, M. Zhang, H. Chen, Y. Liu, L. Liu, X. Gong, B. Jiang, J. Ma and J. Zheng, *ACS Omega*, 2017, **2**, 784-792.
21. M. Baram, Y. Atsmon-Raz, B. Ma, R. Nussinov and Y. Miller, *Physical Chemistry Chemical Physics*, 2016, **18**, 2330-2338.
22. Y. Raz and Y. Miller, *PLoS One*, 2013, **8**, e73303.
23. Y. Atsmon-Raz and Y. Miller, *The Journal of Physical Chemistry B*, 2016, **120**,

10649-10659.
24. M. I. Ivanova, Y. Lin, Y.-H. Lee, J. Zheng and A. Ramamoorthy, *Biophysical Chemistry*, 2020, 106507.
25. P. Bharadwaj, T. Solomon, B. R. Sahoo, K. Ignasiak, S. Gaskin, J. Rowles, G. Verdile, M. J. Howard, C. S. Bond and A. Ramamoorthy, *Scientific reports*, 2020, **10**, 1-14.
26. L. Ostermeier, G. A. de Oliveira, W. Dzwolak, J. L. Silva and R. Winter, *Biophysical Chemistry*, 2020, **268**, 106506.
27. K. Hartman, J. R. Brender, K. Monde, A. Ono, M. L. Evans, N. Popovych, M. R. Chapman and A. Ramamoorthy, *PeerJ*, 2013, **1**, e5.
28. R. T. Johnson, *The Lancet Neurology*, 2005, **4**, 635-642.
29. S. B. Prusiner, *Annual review of genetics*, 2013, **47**, 601-623.
30. F. O. Bastian, *Journal of Alzheimer's Disease*, 2017, **56**, 867-873.
31. J. A. Hainfellner, J. Wanschitz, K. Jellinger, P. P. Liberski, F. Gullotta and H. Budka, *Acta neuropathologica*, 1998, **96**, 116-122.
32. G. De Brito, F. C. Lupinacci, F. H. Beraldo, T. G. Santos, M. Roffé, M. H. Lopes, V. C. De Lima, V. R. Martins and G. N. Hajj, *Biochemical Journal*, 2017, **474**, 2981-2991.
33. A. Strom, B. Yutzy, C. Kruip, I. Völker, N. Schloot, M. Roden, F. Scott, J. Löwer and E. Holznagel, *Veterinary pathology*, 2013, **50**, 909-913.
34. C.-M. Wang and B. Kaltenboeck, *World journal of diabetes*, 2010, **1**, 27.
35. N. Pham, A. Dhar, S. Khalaj, K. Desai and C. Taghibiglou, *Biochemical and Biophysical Research Communications*, 2014, **448**, 151-156.
36. N. T. Vagelatos and G. D. Eslick, *Epidemiologic reviews*, 2013, **35**, 152-160.
37. P. Brundin, R. Melki and R. Kopito, *Nature reviews Molecular cell biology*, 2010, **11**, 301-307.
38. A. Mukherjee, D. Morales-Scheihing, N. Salvadores, I. Moreno-Gonzalez, C. Gonzalez, K. Taylor-Presse, N. Mendez, M. Shahnawaz, A. O. Gaber and O. M. Sabek, *Journal of Experimental Medicine*, 2017, **214**, 2591-2610.
39. Z. Jaunmuktane, S. Mead, M. Ellis, J. D. Wadsworth, A. J. Nicoll, J. Kenny, F. Launchbury, J. Linehan, A. Richard-Loendt and A. S. Walker, *Nature*, 2015, **525**, 247-250.
40. A. Mukherjee and C. Soto, *Cold Spring Harbor perspectives in medicine*, 2017, **7**, a024315.
41. M. Guentchev, T. Voigtländer, C. Haberler, M. H. Groschup and H. Budka, *Neurobiology of disease*, 2000, **7**, 270-273.
42. A. Aguzzi, C. Sigurdson and M. Heikenwaelder, *Annual Review of Pathology: Mechanisms of Disease*, 2008, **3**, 11-40.
43. T. E. Rocke, *Journal of endocrinology*, 2008, **197**, 251-263.
44. C.-Y. King, P. Tittmann, H. Gross, R. Gebert, M. Aebi and K. Wüthrich, *Proceedings of the National Academy of Sciences*, 1997, **94**, 6618-6622.
45. K. E. Marshall, M. R. Hicks, T. L. Williams, S. V. Hoffmann, A. Rodger, T. R. Dafforn and L. C. Serpell, *Biophysical journal*, 2010, **98**, 330-338.
46. J. J. Balbach, Y. Ishii, O. N. Antzutkin, R. D. Leapman, N. W. Rizzo, F. Dyda, J.

Reed and R. Tycko, *Biochemistry*, 2000, **39**, 13748-13759.
47. M. R. Sawaya, S. Sambashivan, R. Nelson, M. I. Ivanova, S. A. Sievers, M. I. Apostol, M. J. Thompson, M. Balbirnie, J. J. Wiltzius and H. T. McFarlane, *Nature*, 2007, **447**, 453.
48. J.-P. Colletier, A. Laganowsky, M. Landau, M. Zhao, A. B. Soriaga, L. Goldschmidt, D. Flot, D. Cascio, M. R. Sawaya and D. Eisenberg, *Proceedings of the National Academy of Sciences*, 2011, **108**, 16938-16943.
49. K. Tenidis, M. Waldner, J. Bernhagen, W. Fischle, M. Bergmann, M. Weber, M.-L. Merkle, W. Voelter, H. Brunner and A. Kapurniotu, *Journal of molecular biology*, 2000, **295**, 1055-1071.
50. C. Bleiholder, N. F. Dupuis, T. Wyttenbach and M. T. Bowers, *Nature chemistry*, 2011, **3**, 172-177.
51. L. Esposito, C. Pedone and L. Vitagliano, *Proceedings of the National Academy of Sciences*, 2006, **103**, 11533-11538.
52. J. Zheng, B. Ma, C.-J. Tsai and R. Nussinov, *Biophysical journal*, 2006, **91**, 824-833.
53. P. C. A. van der Wel, J. R. Lewandowski and R. G. Griffin, *Biochemistry*, 2010, **49**, 9457-9469.
54. R. Diaz-Avalos, C. Long, E. Fontano, M. Balbirnie, R. Grothe, D. Eisenberg and D. L. Caspar, *Journal of molecular biology*, 2003, **330**, 1165-1175.
55. M. Landau, M. R. Sawaya, K. F. Faull, A. Laganowsky, L. Jiang, S. A. Sievers, J. Liu, J. R. Barrio and D. Eisenberg, *PLoS biology*, 2011, **9**, e1001080.
56. A. B. Soriaga, S. Sangwan, R. Macdonald, M. R. Sawaya and D. Eisenberg, *The Journal of Physical Chemistry B*, 2016, **120**, 5810-5816.
57. J. J. Wiltzius, M. Landau, R. Nelson, M. R. Sawaya, M. I. Apostol, L. Goldschmidt, A. B. Soriaga, D. Cascio, K. Rajashankar and D. Eisenberg, *Nature structural molecular biology*, 2009, **16**, 973-979.
58. H. H. G. Tsai, M. Reches, C. J. Tsai, K. Gunasekaran, E. Gazit and R. Nussinov, *Proceedings of the National Academy of Sciences*, 2005, **102**, 8174-8179.
59. T. Lührs, C. Ritter, M. Adrian, D. Riek-Loher, B. Bohrmann, H. Döbeli, D. Schubert and R. Riek, *Proceedings of the National Academy of Sciences*, 2005, **102**, 17342-17347.
60. S. Luca, W. M. Yau, R. Leapman and R. Tycko, *Biochemistry*, 2007, **46**, 13505-13522.
61. M. Zhang, R. Hu, H. Chen, Y. Chang, J. Ma, G. Liang, J. Mi, Y. Wang and J. Zheng, *PCCP*, 2015, **17**, 23245-23256.
62. M. Zhang, R. Hu, H. Chen, X. Gong, F. Zhou, L. Zhang and J. Zheng, *Journal of chemical information modeling*, 2015, **55**, 1628-1639.
63. I. Moreno-Gonzalez, G. Edwards III, N. Salvadores, M. Shahnawaz, R. Diaz-Espinoza and C. Soto, *Molecular psychiatry*, 2017, **22**, 1327-1334.
64. W. Han and C. Li, *Proceedings of the National Academy of Sciences*, 2010, **107**, 6557-6558.
65. C. Infante-Garcia, J. J. Ramos-Rodriguez, L. Galindo-Gonzalez and M. Garcia-Alloza, *Psychoneuroendocrinology*, 2016, **65**, 15-25.

66. X. Yu and J. Zheng, *PLoS One*, 2011, **6**, e20575.
67. X. Yu, Q. Wang and J. Zheng, *Biophysical Journal*, 2010, **99**, 666-674.
68. M. Z. Zhang, R. D. Hu, G. Z. Liang, Y. Chang, Y. Sun, Z. M. Peng and J. Zheng, *J Phys Chem B*, 2014, **118**, 7026-7036.
69. J. Zhao, X. Yu, G. Liang and J. Zheng, *Biomacromolecules*, 2011, **12**, 210-220.
70. P. C. A. van der Wel, J. R. Lewandowski and R. G. Griffin, *Journal of the American Chemical Society*, 2007, **129**, 5117-5130.
71. G. Fusco, S. W. Chen, P. T. Williamson, R. Cascella, M. Perni, J. A. Jarvis, C. Cecchi, M. Vendruscolo, F. Chiti and N. Cremades, *Science*, 2017, **358**, 1440-1443.
72. S. De, D. C. Wirthensohn, P. Flagmeier, C. Hughes, F. A. Aprile, F. S. Ruggeri, D. R. Whiten, D. Emin, Z. Xia and J. A. Varela, *Nature communications*, 2019, **10**, 1-11.
73. M. W. Ullah, S. Manan, Z. Guo and G. Yang, *Engineered Science*, 2020, **10**, 8-10.
74. V. S. Shaikh, Y. I. Shaikh and K. Ahmed, *Engineered Science*, 2020, **12**, 113-118.
75. V. S. Shaikh, G. M. Nazeruddin, Y. I. S. S. H. Bloukh, Z. Edis and H. M. Pathan, *Engineered Science*, 2020, **10**, 11-23.
76. X. Bu, Y. Xiang, W. Jin, J. Wang, L. Shen, Z. Huang, K. Zhang, Y. Liu, F. Zeng and J. Liu, *Molecular psychiatry*, 2018, **23**, 1948-1956.
77. C. Soto, *Cell*, 2012, **149**, 968-977.
78. J. Canet-Ferrer, E. Coronado, A. Forment-Aliaga and E. Pinilla-Cienfuegos, *Nanotechnology*, 2014, **25**, 395703.
79. A. Micsonai, F. Wien, L. Kernya, Y.-H. Lee, Y. Goto, M. Réfrégiers and J. Kardos, *Proceedings of the National Academy of Sciences*, 2015, **112**, E3095-E3103.
80. S. Löfås and B. Johnsson, *Chemical Communications*, 1990, 1526-1528.
81. S. D. Krämer, J. Wöhrle, C. Rath and G. Roth, *Bioinformatics and Biology Insights*, 2019, **13**, 1177932218821383.
82. E. Hellstrand, A. Nowacka, D. Topgaard, S. Linse and E. Sparr, *PLoS One*, 2013, **8**, e77235.
83. B. Ren, Y. Liu, Y. Zhang, Y. Cai, X. Gong, Y. Chang, L. Xu and J. Zheng, *ACS Chemical Neuroscience*, 2018, **9**, 1215-1224.
84. G. Van Meer, D. R. Voelker and G. W. Feigenson, *Nature reviews Molecular cell biology*, 2008, **9**, 112-124.
85. E. Strandberg, D. Tiltak, S. Ehni, P. Wadhwani and A. S. Ulrich, *Biochimica et Biophysica Acta -Biomembranes*, 2012, **1818**, 1764-1776.
86. R. Nelson, M. R. Sawaya, M. Balbirnie, A. Ø. Madsen, C. Riekel, R. Grothe and D. Eisenberg, *Nature*, 2005, **435**, 773-778.
87. L. Kale, R. Skeel, M. Bhandarkar, R. Brunner, A. Gursoy, N. Krawetz, J. Phillips, A. Shinozaki, K. Varadarajan and K. Schulten, *Journal of Computational Physics*, 1999, **151**, 283-312.
88. A. D. MacKerell, D. Bashford, M. Bellott, R. L. Dunbrack, J. D. Evanseck, M. J. Field, S. Fischer, J. Gao, H. Guo, S. Ha, D. Joseph-McCarthy, L. Kuchnir, K. Kuczera, F. T. K. Lau, C. Mattos, S. Michnick, T. Ngo, D. T. Nguyen, B.

Prodhom, W. E. Reiher, B. Roux, M. Schlenkrich, J. C. Smith, R. Stote, J. Straub, M. Watanabe, J. Wiorkiewicz-Kuczera, D. Yin and M. Karplus, *The Journal of Physical Chemistry B*, 1998, **102**, 3586-3616.

89. W. Humphrey, A. Dalke and K. Schulten, *Journal of Molecular Graphics*, 1996, **14**, 33-38.